Journal of Sound and Vibration 626 (2026) 119614

Contents lists available at ScienceDirect

Journal of Sound and Vibration

journal homepage: www.elsevier.com/locate/jsvi

Broadband vibration reduction through combined linear-nonlinear oscillators in a meta-plate

Chen Gong [a], Xin Fang [b,*], Hangxing Li [a], Zhiyuan Li [a], Li Cheng [a,*]

[a] Department of Mechanical Engineering, Hong Kong Polytechnic University, Hong Kong, China
[b] Laboratory of Science and Technology on Integrated Logistics Support, College of Intelligent Science, National University of Defense Technology, Changsha, Hunan 410073, China

ARTICLE INFO

Keywords:
Nonlinear meta-materials/structures
Chaotic band
Bandgaps
Vibro-impact oscillators

ABSTRACT

Nonlinear acoustic meta-materials/structures (NAMs) hold great promise for ultra-low and ultra-broadband vibration suppression through chaotic band mechanisms, but at the expense of compromising the original bandgap benefits. To concurrently harness the benefits arising from both bandgaps and chaotic passbands, we propose a dedicated design paradigm in which both linear and nonlinear oscillators are integrated in meta-plates. Harmonic balance method and time-domain integration are utilized to compute the system responses and evaluate the performances of two types of meta-plates. Type I design leverages the complementary benefits of linear acoustic meta-materials/structures (LAMs) and NAMs. The design entails the stability of the bandgap, in which additional 17 dB improvement is achieved over traditional NAMs, while maintaining a stable chaotic band. Type II extends the Type I design, elucidating the influence of nonlinearity location, linear stiffness and damping. Based on the insights gained, broadband vibration suppression has seen a significant extension into the lower frequency range, along with a notable improvement in vibration suppression effectiveness. Our concept is demonstrated experimentally on a meta-plate consisting of linear and vibro-impact nonlinear oscillators. The study alludes to a new route for designing high-performance meta-structures in views of structural vibration control.

1. Introduction

Acoustic metamaterials (AMs) and metastructures, designed for controlling low-frequency elastic waves, can be customized by strategically tailoring the constituent artificial microstructural units [1–5]. NAMs [6–12], incorporating nonlinear local resonators, have garnered increasing attention due to their unique properties unattainable in their linear counterparts. For instance, NAMs can achieve nonreciprocal wave propagation [13,14] and break the mass law governing the sound insulation for conventional structures [15]. Crucially, they can enable ultra-low and ultrabroad-band wave suppression, thereby overcoming the narrow-band limitations

Abbreviations: NAMs, nonlinear acoustic meta-materials/structures; LAMs, linear acoustic meta-materials/structures; AMs, acoustic meta-materials; LR, local resonant; LM, linear model for type I and type II; LM&NM, linear and nonlinear model for type I; LM&NM 1, linear and nonlinear model 1 for type II; LM&NM 2, linear and nonlinear model 2 for type II; NM, nonlinear model for type I and type II; AMM, assumed modes method; FEM, finite element method.

* Corresponding authors.
E-mail addresses: xinfangdr@sina.com (X. Fang), li.cheng@polyu.edu.hk (L. Cheng).

https://doi.org/10.1016/j.jsv.2025.119614
Received 25 September 2025; Received in revised form 3 December 2025; Accepted 15 December 2025
Available online 16 December 2025

inherent to LAMs [16] and offering new avenues for vibration mitigation [17–20] and sound radiation control [17,21–23].

As demonstrated in the literature, the chaotic band in NAMs is an essential mechanism for achieving the broadband vibration reduction [24–26]. Inside these bands, incident periodic waves can be converted into chaotic transmitted waves [24]. In NAMs with hardening nonlinearity, chaotic bands can effectively reduce the vibration transmission above the nonlinear resonant bandgaps [26]. This reduction effect remains insensitive to the mass ratio of the local resonators, enabling lightweight and optimized designs [25]. Research has further clarified the influence of design parameters on NAM-induced vibration reduction performance [27], spurring the development of dedicated NAM unit cells, which are engineered to generate strong nonlinearity under moderate excitation amplitudes [28–30]. Experimental validation has also confirmed the exceptional ultra-low and ultra-broadband vibration suppression achieved through chaotic bands in NAM-based beams and plates [16,17]. Subsequent applications have successfully implemented this strategy in honeycomb sandwich plates [18] and cantilever wing plates [31,32] for mitigating aeroelastic vibration in high-speed flow [19,20]. Further advancing this field, Yu et al. demonstrated that combining vibro-impact motion with proper damping can produce a robust hyper-damping effect, thereby substantially augmenting the vibration reduction potential of NAMs [33,34].

Although chaotic bands are shown to provide effective vibration suppression within NAMs' passbands, the beneficial nonlinear effects arising come at a cost: they impair the performance of locally resonant (LR) bandgaps [24–26], which can also be beneficial in many applications such as vibration reduction, sound absorption and wave control. Bandgaps in NAMs are dominated by the degeneration of dispersion curves [13,46] and self-adaptivity of the reduction range [28,46], both stemming from the time-space amplitude-dependent properties of NAMs [35–45]. When increasing the excitation amplitude, the NAM bandgap shifts downward/upward for softening/hardening nonlinearity [35]. In weakly NAMs structures [35,44], the bending of the dispersion curves reflects the degeneration (narrowing) of bandgaps as nonlinearity strengthens. In strongly NAMs [46], bandgaps are exemplified by the shortening, merging, or even disappearance of dispersion curves. These changes are driven by the varying nonlinear strength, which induce transitions in wave modes and consequently lead to bandgap degeneration. On the other hand, the bandwidth of the total LR bandgap is self-adaptive with the propagation distance and time, because the reduced wave amplitude shifts the bandgap range during the wave propagation process, causing the sweeping of the bandgap effect across a broad frequency range, thereby leading to ultrabroad bandgaps [28,46]. In high-dimensional NAM structures [13], spatial divergence can accelerate this self-adaptivity process. Consequently, it is difficult for NAMs to sustain stable bandgaps under excitations with varying amplitude or in large-scale and higher-dimensional structures. In contrast, one of the appealing features of the LAM bandgaps is their proven ability to suppress vibrations regardless of the external excitation intensity [47–49]. Also, the vibration reduction level within chaotic bands is usually lower than that inside the bandgap [24]. Thus, leveraging the advantages of both LAM and NAM through combining linear and nonlinear oscillators in structural design might be a solution to maintain both ultra-deep bandgaps and ultra-broad chaotic bands simultaneously. Earlier work has shown that subwavelength nonreciprocal elastic diodes can be realized via combining linear and nonlinear AMs [13,14]. For vibration reduction, numerical studies also confirmed the efficacy of a combined design in a 1D NAM chain using gradient nonlinear stiffness coefficients [50]. However, this strategy has not yet been exploited in high-dimensional NAM structures, alongside the lack of experimental demonstration and analysis of the underlying physical mechanisms.

To tackle these problems, this paper investigates a high-dimensional meta-plate which incorporates both linear and nonlinear local oscillators. We develop a comprehensive modeling framework for the meta-plate, predict its vibrational responses, define evaluation criteria for assessing vibration reduction performance, and validate the approach through time-domain simulations. The study investigates two distinct combinational systems of LAMs and NAMs: Type I utilizes equal-frequency oscillators while Type II involves different-frequency oscillators. We further fabricate a meta-plate and experimentally demonstrate its performance and elucidate the underlying physical mechanisms, thereby bridging the gap in the field of NAMs.

2. Nonlinear meta-plate and analysis methods

Fig. 1(a) illustrates a nonlinear meta-plate consisting of a rectangular thin plate, over which 5×6 periodic metacells are installed. The substrate plate is made of aluminum alloy with dimensions $a \times b \times h = 0.7 \times 0.84 \times 0.006$ m, density $\rho = 2700$ kg/m^3, Young's modulus $E = 67$ GPa, and Poisson's ratio $\nu = 0.3$, respectively. The metacell is square, with a lattice constant of 0.04 m. These parameters can form

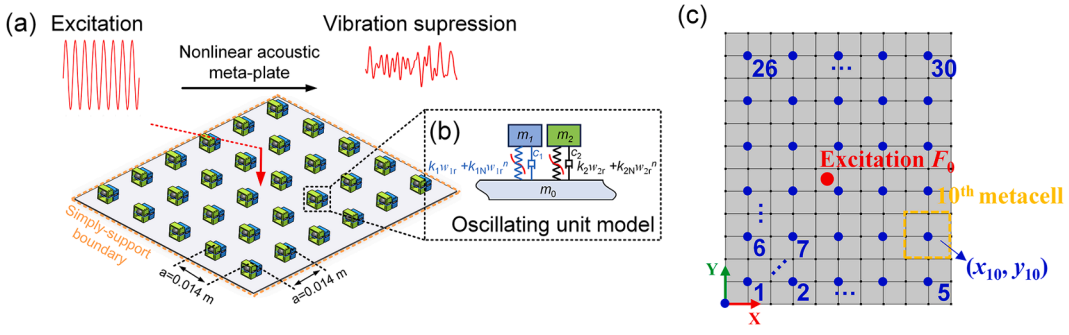

Fig. 1. Metamaterial model. (a) Schematic of an finite plate with 30 periodically arranged nonlinear oscillators. (b) Equivalent model of the nonlinear oscillators. (c) Distribution and positions of the metacells and exctiation.

efficient LR bandgaps in the meta-plate [17,18,48]. As shown in Fig. 1(b), a concentrated mass m_0 is embedded on the plate and coupled to two independent oscillators with masses m_1, m_2, linear stiffness k_1, k_2 and damping coefficients c_1, c_2, respectively. The displacements of m_0, m_1 and m_2 denote w_0, w_1 and w_2, respectively. $w_{1r} = w_1\text{-}w_0$ and $w_{2r} = w_2\text{-}w_0$. Natural frequencies are $\omega_i = 2\pi f_i$, $i = 1, 2$; thus, the linear stiffness of individual resonators are $k_i = (\omega_i)^2 m_i$, $i = 1, 2$. The damping coefficient denotes $c_i = 0.01 k_i/\omega_i$ [17]. Damping and geometrical nonlinearity in the plate are not considered; therefore, nonlinearity only arises from the local oscillators, with k_{1N} and k_{2N} denoting the nonlinear stiffness coefficients ($k_{1N} = k_{2N}$). Thus, the equation of motion for the s^{th} ($s = 1, 2, \ldots, 30$) metacell is given by:

$$\begin{cases} m_0\ddot{w}(x_s,y_s,t) - k_1 w_{1r}^s - k_{1N}\left(w_{1r}^s\right)^n - k_2 w_{2r}^s - k_{2N}\left(w_{2r}^s\right)^n = F_s(x_s,y_s) \\ m_1\left(\ddot{w}(x_s,y_s,t) + \ddot{w}_{1r}^s\right) + k_1 w_{1r}^s + k_{1N}\left(w_{1r}^s\right)^3 = 0 \\ m_2\left(\ddot{w}(x_s,y_s,t) + \ddot{w}_{2r}^s\right) + k_2 w_{2r}^s + k_{2N}\left(w_{2r}^s\right)^3 = 0 \end{cases}, \tag{1}$$

where n is a nonlinear factor that can be achieved through oscillating unit design [29]. Here, we adopt the cubic stiffness nonlinearity ($n = 3$), as used in many studies [13,28,46], to show the salient phenomena in the system. The nonlinear stiffness coefficients are specified as $k_{1N} = 0$ or $k_{2N} = 1 \times 10^{13}$ N/m^3 to ensure the occurrence of the chaotic bands under a moderate excitation level [17,18].

Without nonlinearity, the meta-plate exhibits two distinct band structure configurations: one LR bandgap with two passbands (achieved when $f_1 = f_2$); and two LR bandgaps with three passbands (achieved when $f_1 \neq f_2$). Consequently, we define two system types: Type I with $f_1 = f_2$ and Type II with $f_1 \neq f_2$. Each type implements four design strategies: Linear model (LM, $k_{1N} = k_{2N} = 0$); Linear and nonlinear model 1 (LM&NM 1, $k_{1N} = 0$ and $k_{2N} = 1 \times 10^{13}$ N/m^3); Linear and nonlinear model 2 (LM&NM 2, $k_{1N} = 1 \times 10^{13}$ and $k_{2N} = 0$ N/m^3); Dual nonlinear model (NM, $k_{1N} = k_{2N} = 1 \times 10^{13}$ N/m^3). For Type I systems ($f_1 = f_2$), LM&NM 1 and LM&NM 2 models are equivalent due to oscillator symmetry; thus, they are collectively denoted as LM&NM. The following sections investigate the vibration suppression characteristics and the underlying physical mechanisms of both system types. Based on these findings, we develop tailored design strategies to cope with diverse vibration suppression requirements.

2.1. Modelling of the meta-plate

The vibration of 30-metacell-loaded meta-plate system is characterized by the vibration of the thin plate subjected to the reaction forces [F_1, F_2, …, F_{30}] from the metacells and an external excitation force. Coupled with Eq. (1), the equation governing the entire meta-plate system motion writes:

$$\begin{cases} \rho h\dfrac{\partial^2 w(x,y,t)}{\partial t^2} + D\left(\dfrac{\partial^4 w(x,y,t)}{\partial x^4} + 2\dfrac{\partial^4 w(x,y,t)}{\partial x^2 y^2} + \dfrac{\partial^4 w(x,y,t)}{\partial y^4}\right) \\ = -F_1(x_1,y_1)\delta(x-x_1)\delta(y-y_1) - F_2(x_2,y_2)\delta(x-x_2)\delta(y-y_2) - \ldots \\ -F_{30}\left(x_{30},y_{30}\right)\delta(x-x_{30})\delta\left(y-y_{30}\right) + F_0\sin(2\pi f t)\delta(x-x_c)\delta(y-y_c) \\ m_0\ddot{w}(x_1,y_1,t) - k_1 w_{1r}^1 - k_{1N}\left(w_{1r}^1\right)^3 - k_2 w_{2r}^1 - k_{2N}\left(w_{2r}^1\right)^3 = F_1(x_1,y_1) \\ m_1\left(\ddot{w}(x_1,y_1,t) + \ddot{w}_{1r}^1\right) + k_1 w_{1r}^1 + k_{1N}\left(w_{1r}^1\right)^3 = 0 \\ m_2\left(\ddot{w}(x_1,y_1,t) + \ddot{w}_{2r}^1\right) + k_2 w_{2r}^1 + k_{2N}\left(w_{2r}^1\right)^3 = 0 \\ \ldots \\ m_0\ddot{w}\left(x_{30},y_{30},t\right) - k_1 w_{1r}^{30} - k_{1N}\left(w_{1r}^{30}\right)^3 - k_2 w_{2r}^{30} - k_{2N}\left(w_{2r}^{30}\right)^{30} = F_{30}\left(x_{30},y_{30}\right) \\ m_1\left(\ddot{w}\left(x_{30},y_{30},t\right) + \ddot{w}_{1r}^{30}\right) + k_1 w_{1r}^{30} + k_{1N}\left(w_{1r}^{30}\right)^3 = 0 \\ m_2\left(\ddot{w}\left(x_{30},y_{30},t\right) + \ddot{w}_{2r}^{30}\right) + k_2 w_{2r}^{30} + k_{2N}\left(w_{2r}^{30}\right)^3 = 0 \end{cases}, \tag{2}$$

where w denotes the transverse plate displacement; $D = \frac{Eh^3}{12(1-\nu^2)}$ represents the flexural stiffness; (x_s, y_s) denotes the location of the s^{th} ($s = 1, 2, \ldots, 30$) metacell; δ is the Dirac delta function; F_0, f and (x_c, y_c) specify the excitation amplitude, frequency and location, respectively.

Eq. (2) is solved via modal superposition (Assumed Modes Method (AMM)). Assuming the natural frequencies ω_{ij} and the corresponding mode shape functions$\phi_{ij}(x,y)$, the displacement solution considering $m_c \times n_c$ modes is expressed as:

$$w(x,y,t) = \sum_{i=1}^{m_c}\sum_{j=1}^{n_c}\phi_{ij}(x,y)q_{ij}(t). \tag{3}$$

For simply-supported boundary conditions as shown in Fig. 1(a), mode shape functions $\phi_{ij}(x,y)$ are analytically known as:

$$\phi_{ij} = \sin\left(\frac{i\pi x}{a}\right)\sin\left(\frac{j\pi y}{b}\right)\ (i=1,2,\ldots,m_c; j=1,2,\ldots,n_c). \tag{4}$$

Substituting Eq. (3) into Eq. (2) yields:

$$\begin{cases}
\sum_{i=1}^{m_c}\sum_{j=1}^{n_c}\rho h\phi_{ij}(x,y)\ddot{q}_{ij}(t) + \sum_{i=1}^{m_c}\sum_{j=1}^{n_c}D\left(\frac{\partial^4\phi_{ij}(x,y)}{\partial x^4} + 2\frac{\partial^4\phi_{ij}(x,y)}{\partial x^2 y^2} + \frac{\partial^4\phi_{ij}(x,y)}{\partial y^4}\right)q_{ij}(t) \\
= -F_1(x_1,y_1)\delta(x-x_1)\delta(y-y_1) - F_2(x_2,y_2)\delta(x-x_2)\delta(y-y_2) - \ldots \\
-F_{30}(x_{30},y_{30})\delta(x-x_{30})\delta(y-y_{30}) + F_0\sin(2\pi ft)\delta(x-x_c)\delta(y-y_c) \\
m_0\sum_{i=1}^{m_c}\sum_{j=1}^{n_c}\phi_{ij}(x_1,y_1)\ddot{q}_{ij}(t) - c_1\dot{w}_{1r}^1 - k_1 w_{1r}^1 - k_{1N}\left(w_{1r}^1\right)^3 - c_2\dot{w}_{2r}^1 - k_2 w_{2r}^1 - k_{2N}\left(w_{2r}^1\right)^3 = F_1(x_1,y_1) \\
m_1\left(\sum_{i=1}^{m_c}\sum_{j=1}^{n_c}\phi_{ij}(x_1,y_1)\ddot{q}_{ij}(t) + \ddot{w}_{1r}^1\right) + c_1\dot{w}_{1r}^1 + k_1 w_{1r}^1 + k_{1N}\left(w_{1r}^1\right)^3 = 0 \\
m_2\left(\sum_{i=1}^{m_c}\sum_{j=1}^{n_c}\phi_{ij}(x_1,y_1)\ddot{q}_{ij}(t) + \ddot{w}_{2r}^1\right) + c_2\dot{w}_{2r}^1 + k_2 w_{2r}^1 + k_{2N}\left(w_{2r}^1\right)^3 = 0 \\
\ldots \\
m_0\sum_{i=1}^{m_c}\sum_{j=1}^{n_c}\phi_{ij}(x_{30},y_{30})\ddot{q}_{ij}(t) - c_1\dot{w}_{1r}^{30} - k_1 w_{1r}^{30} - k_{1N}\left(w_{1r}^{30}\right)^3 - c_2\dot{w}_{2r}^{30} - k_2 w_{2r}^{30} - k_{2N}\left(w_{2r}^{30}\right)^3 = F_{30}(x_{30},y_{30}) \\
m_1\left(\sum_{i=1}^{m_c}\sum_{j=1}^{n_c}\phi_{ij}(x_{30},y_{30})\ddot{q}_{ij}(t) + \ddot{w}_{1r}^{30}\right) + c_1\dot{w}_{1r}^{30} + k_1 w_{1r}^{30} + k_{1N}\left(w_{1r}^{30}\right)^3 = 0 \\
m_2\left(\sum_{i=1}^{m_c}\sum_{j=1}^{n_c}\phi_{ij}(x_{30},y_{30})\ddot{q}_{ij}(t) + \ddot{w}_{2r}^{30}\right) + c_2\dot{w}_{2r}^{30} + k_2 w_{2r}^{30} + k_{2N}\left(w_{2r}^{30}\right)^3 = 0
\end{cases} \tag{5}$$

Multiplying both sides of the first formula in Eq. (5) by the mode shape function of index p and q, integrating over the entire plate area and making use of the orthogonality properties of the mode shapes give the coupled equation of the system, expresses in matrix form as (detailed matrix expressions provided in Appendix A.1):

$$\mathbf{M}\ddot{\mathbf{Q}} + \mathbf{C}\dot{\mathbf{Q}} + \mathbf{K}\mathbf{Q} + \mathbf{K_d}\mathbf{Q}^3 = \mathbf{F}, \tag{6}$$

where $\mathbf{Q} = [q_{11}, q_{12},\ldots, q_{mcnc}, w_{1r}^1, w_{2r}^1,\ldots, w_{1r}^{30}, w_{2r}^{30}]^T$. The above equation is solved using the harmonic balance method. Due to the cubic nonlinearity of the system, the one-third and third harmonic components are dominant among all subharmonic and super-harmonic responses. Thus, the steady-state response is assumed to take the form:

$$\mathbf{Q} = \mathbf{A}_1\sin\left(\frac{1}{3}\omega t\right) + \mathrm{B}_1\cos\left(\frac{1}{3}\omega t\right) + \mathbf{C}_1\sin(\omega t) + \mathbf{D}_1\cos(\omega t) + \mathbf{E}_1\sin(3\omega t) + \mathbf{F}_1\cos(3\omega t). \tag{7}$$

Substituting Eq. (7) into (6) and balancing the coefficients in front of the sinsoidal function terms give:

$$\begin{cases}
\left[\mathbf{K} - \frac{1}{9}\omega^2\mathbf{M}\right]\mathbf{A}_1 - \frac{1}{3}\omega\mathbf{C}\mathbf{B}_1 + \mathbf{K_d}\boldsymbol{\alpha}_1 = \mathbf{0} \\
\left[\mathbf{K} - \frac{1}{9}\omega^2\mathbf{M}\right]\mathbf{B}_1 + \frac{1}{3}\omega\mathbf{C}\mathbf{A}_1 + \mathbf{K_d}\boldsymbol{\alpha}_2 = \mathbf{0} \\
\left[\mathbf{K} - \omega^2\mathbf{M}\right]\mathbf{C}_1 - \omega\mathbf{C}\mathbf{D}_1 + \mathbf{K_d}\boldsymbol{\alpha}_3 = \mathbf{F_0} \\
\left[\mathbf{K} - \omega^2\mathbf{M}\right]\mathbf{D}_1 + \omega\mathbf{C}\mathbf{C}_1 + \mathbf{K_d}\boldsymbol{\alpha}_4 = \mathbf{0} \\
\left[\mathbf{K} - 9\omega^2\mathbf{M}\right]\mathbf{E}_1 - 3\omega\mathbf{C}\mathbf{F}_1 + \mathbf{K_d}\boldsymbol{\alpha}_5 = \mathbf{0} \\
\left[\mathbf{K} - 9\omega^2\mathbf{M}\right]\mathbf{F}_1 + 3\omega\mathbf{C}\mathbf{E}_1 + \mathbf{K_d}\boldsymbol{\alpha}_6 = \mathbf{0}
\end{cases} \tag{8}$$

where detailed expressions of $\mathbf{A}_1$, $\mathbf{B}_1$, $\mathbf{C}_1$, $\mathbf{D}_1$, $\mathbf{E}_1$ $\mathbf{F}_1$, $\boldsymbol{\alpha}_1$, $\boldsymbol{\alpha}_2$, $\boldsymbol{\alpha}_3$, $\boldsymbol{\alpha}_4$, $\boldsymbol{\alpha}_5$ and $\boldsymbol{\alpha}_6$ are provided in Appendix A.1.

Vibration responses of the plate are evaluated under an force excitation at ($x_c = 0.385$ m, $y_c = 0.315$ m), as shown in Fig. 1(c). The input point is eccentrical to excite both symmetrical and asymmetrical vibration modes. The solution of $\mathbf{A}_1$, $\mathbf{B}_1$, $\mathbf{C}_1$, $\mathbf{D}_1$, $\mathbf{E}_1$ and $\mathbf{F}_1$ in Eq.

(8) are obtained by the Newton iteration, and their initial values are set to **0** for a given excitation frequency $f \in [0, 1000]$ Hz ($f = \omega/2\pi$). Subsequently, **Q** is derived from Eq. (7). According to Eq. (3), the displacement response can be obtained at any position of the meta-plate.

2.2. Evaluation criteria

The overall vibration level V of the meta-plate is quantified by

$$V(f) = \frac{\sqrt{\sum_{i=1}^{30} (V_s(f))^2 S_s / S_{total}}}{F_0}, \tag{9}$$

in which V_s represents the velocity at each metacell location (x_s, y_s) ($s = 1, 2, \ldots, 30$). A detailed description of sampling points amount is provided in Appendix A.2. The average vibration transmission writes:

$$R(f) = 20\log_{10}(V(f)), \tag{10}$$

where S_s and S_{total} are the area of the s^{th} metcell and that of the entire meta-plate, respectively.

We use the Type I system to demonstrate the simulation accuracy of the model in terms of the proposed evaluation criteria. Fig. 2 shows the transmission R for the LM model using the aforementioned AMM with two different modal truncations: $(m_c, n_c) = (10, 12)$ and (20, 24), respectively. For comparison, results from the finite element method (FEM) are also shown by the black curve, as detailed in Appendix A.3. The results obtained by FEM and AMM are in good agreement: Peak frequency deviations are typically $\leq$4 % for (10, 12) in AMM and $\leq$3 % for (20, 24) in AMM. Balancing the computational efficiency and accuracy, $(m_c, n_c) = (20, 24)$ is adopted in AMM in subsequent analyses. Existing errors primarily arise from modal truncation, which neglects the contribution of higher-order modes to the system's dynamic response. In contrast, the numerical computation error—comprising round-off error (from finite-precision calculations) and truncation error (from algorithmic approximations)—is negligible in comparison, given the ~15 decimal digits of precision employed here. In addition, the bandgap frequency range is obtained according to Bloch-Floquet theorem [13, 17], denoted by the shadowed area. The valley of the R is consistent with the bandgap area (99–133 Hz), further verifying the accuracy of the modelling.

Based on the frequency range of the LM bandgap, the transmission R can be divided into three regions: passband before the bandgap; bandgap (shaded area); and the passband after the bandgap, as shown in Fig. 2. We take the minimum value of R within the bandgap valley, denoted as $Rb_{\min}$, to quantify the vibration reduction effect. Conversely, to evaluate the broadband vibration suppression in the passbands, we take the average value of R, denoted as Rp_{mean}. Their expressions are written as:

$$Rb_{\min} = 20\log_{10}\left(\min\left(\sum_{f=f_{\text{bandgap\_start}}}^{f_{\text{bandgap\_end}}} V(f)\right)\right) \text{and } Rp_{\text{mean}} = 20\log_{10}\left(\text{mean}\left(\sum_{f=f_{\text{passband\_start}}}^{f_{\text{passband\_end}}} V(f)\right)\right). \tag{11}$$

Fig. 3 shows the transmission R calculated by AMM for NM and LM&NM with an increasing excitation force F_0. As F_0 tends to 0, nonlinear solutions converge to linear results, evident in the overlapping curves. Following the linear bandgap reference, R is also segmented into three frequency bands as shown in Fig. 3(a–c). According to Eq. (11), $Rb_{\min}$ and Rp_{mean} can be extracted as shown in Fig. 3(d–f). These metrics enable direct comparison of vibration reduction performance across the three Type I design strategies (LM, NM and LM&NM). Detailed analyses of nonlinear phenomena are provided in subsections.

For Type II system ($f_1 \neq f_2$), varying resonant frequencies of the oscillators produce distinct bandgaps. To facilitate cross-case comparison, results are normalized against linear baselines as follows:

$$Ratio\_Rb_{\min} = \min\left(\sum_{f=f_{\text{bandgap\_start}}}^{f_{\text{bandgap\_end}}} V^{LM}(f)\right) \Big/ \min\left(\sum_{f=f_{\text{bandgap\_start}}}^{f_{\text{bandgap\_end}}} V(f)\right),$$

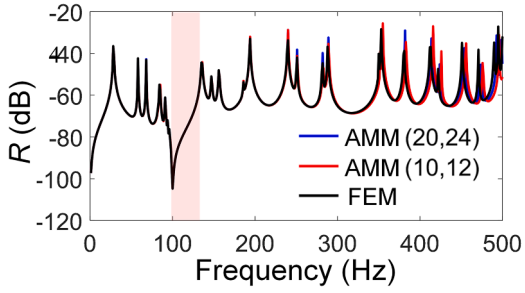

Fig. 2. Transmission R calculated by Eq. (10) for the linear meta-plate by AMM and FEM.

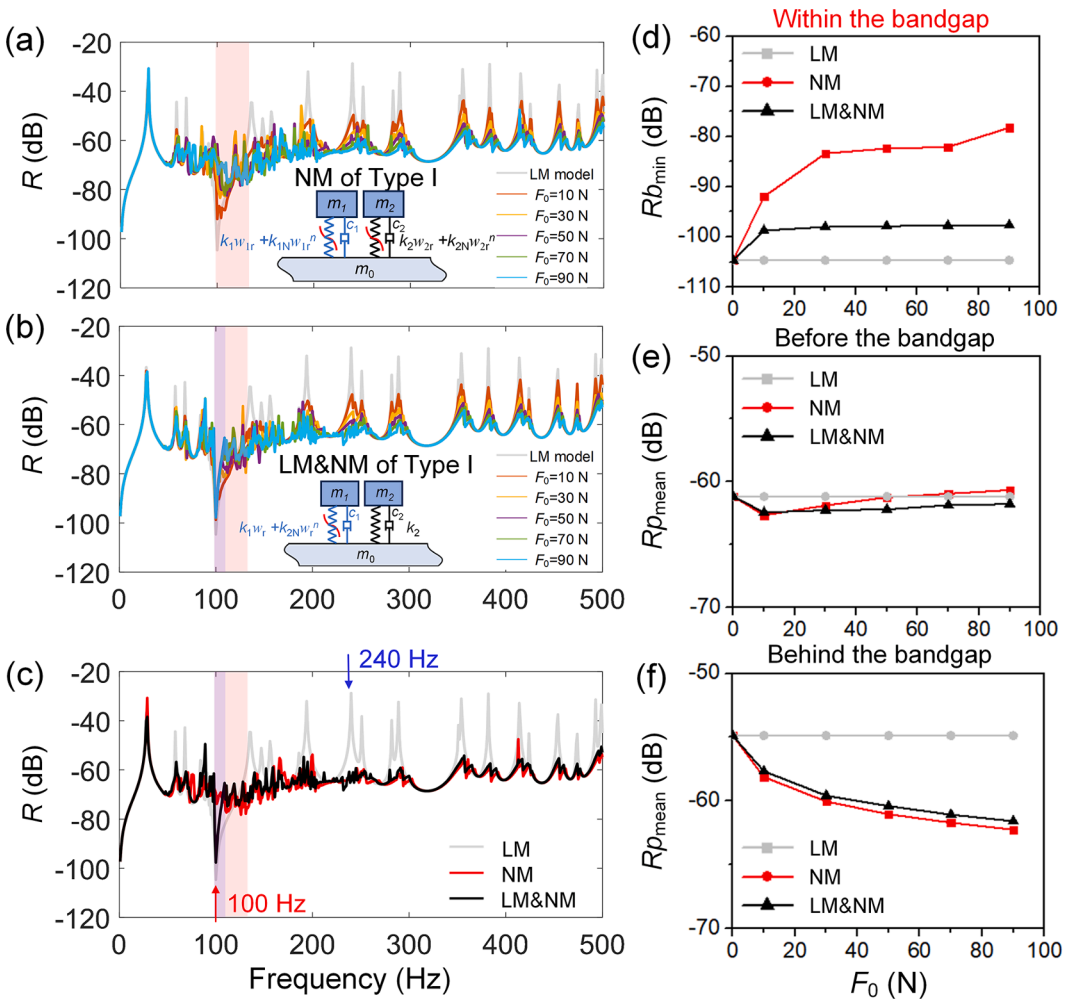

Fig. 3. AMM responses and their statistics datas for the LM, NM and LM&NM models of Type I with increasing F_0. (a) R of NM. (b) R of LM&NM. (c) R of $F_0 = 90$ N (d–f) Comparisions of $Rb_{\min}$ and RP_{mean} among the LM, NM and LM&NM models. (d) is within the bandgap; (e) is before the bandgap; (f) is behind the bandgap.

and

$$Ratio\_Rp_{\mathrm{mean}} = \mathrm{mean}\left(\sum_{f=f_{\mathrm{passband\_start}}}^{f_{\mathrm{passband\_end}}} V^{\mathrm{LM}}(f)\right) \Big/ \mathrm{mean}\left(\sum_{f=f_{\mathrm{passband\_start}}}^{f_{\mathrm{passband\_end}}} V(f)\right). \tag{12}$$

2.3. Validation of the time-domain simuation

To validate AMM predictions, time-domain simuations are performed at typical frequencies. Here, we present examples of NM and LM&NM at two representative excitation frequencies: 100 and 240 Hz. As shown in Fig. 3(c), these two frequencies lie within the bandgap and the passband, respectively. We selecte an integration time of three seconds which is long enough for the system response to reach a steady state at these two frequencies. The last 1 s response is taken as the steady velocity signal for further signal processing such as FFT analysis. Velocity data are collected at 30 measurement points as shown in Fig. 1(c). The spatially averaged velocity $V_{\mathrm{aver}}(f)$ normalized by the excitation force F_0 is shown in Fis. 3(a–d). Meanwhile, the component amplitude $V_s(f)$ are derived from frequency spectra at each metacell location (x_s, y_s) ($s = 1, 2, \ldots, 30$). Following Eq. (9), the numerical $V(f)$ is calculated. Results from the AMM and the time domian numerical model are compared through a normalized index:

$$Ratio(f) = V^{\mathrm{LM}}(f)/V(f), \tag{13}$$

where $V(f)^{\mathrm{LM}}$ denotes $V(f)$ of the LM model.

Consequently, the AMM and numerical $Ratio(100)$ and $Ratio(240)$ are presented in Fig. 4(e, f). At 100 Hz (within the bandgap), the

numerical results for both models exhibit strong agreement with the AMM predictions. At 240 Hz (within the passband), discrepancies emerge between the two sets of results when F_0 reaches 50 N. This divergence stems from the intensified chaotic dynamics induced by increasing nonlinearity [24–26], which exceed the predictive capabilities of the numerical methods. As such, the time-domain signal fails to converge within the three-second simulation window. Despite amplitude deviations, both methods capture a consistent trend. Thus, the time-domain simulations validate the AMM model within the operational amplitude ranges while highlighting limitations under strongly chaotic regimes.

3. Type I system: maintaining both bandgap and chaotic passbands for vibration reduction

For the NM model shown in Fig. 3(a), the identical parameters of masses m_1 and m_2 create a single-degree-of-freedom (1DoF) oscillator system. While most passband peaks (the region behind the red area) are supressed, the bandgap performance (red area) under increasing F_0 can hardly be maintained. To concurrently maintain both bandgap effectiveness and chaotic passband suppression, we reconfigure this 1DoF oascilator as a 2DoF oascialtor system through strategic decoupling: one linear resonator for maintaining the bandgap performance while a parallel nonlinear resonator for enabling chaotic passband suppression. This redesign leads to the LM&NM configuration shown in Fig. 3b

3.1. Vibration reduction by NM versus LM&NM

To evaluate the vibration reduction in the NM model as F_0 increases, we apply the criteria developped in Section 2.2 to both the bandgap and the passband regions. Within the bandgap as shown in Fig. 3(d), $Rb_{\min}$ for NM increases from −105 to −80 dB, while LM remains at −105 dB. Due to the bandgap degeneration [13,46], the NM model loses vibration suppression capability in this region. Within the passbands shown in Fig. 3(e, f), Rp_{mean} remains stable (within 3 dB variation) before the bandgap but decreases from −55 to −63 dB after the bandgap. The selective impact of the nonlinearity on the passband behind the bandgap will be scrutinized at subsquent sections. The NM model achieves broadband passband suppression through chaotic band effects [24–26], with stronger nonlinearity enhancing this suppression.

Despite its broadband performance, NM's bandgap disappearance is undesirable. While chaotic bands suppress resonance peaks,

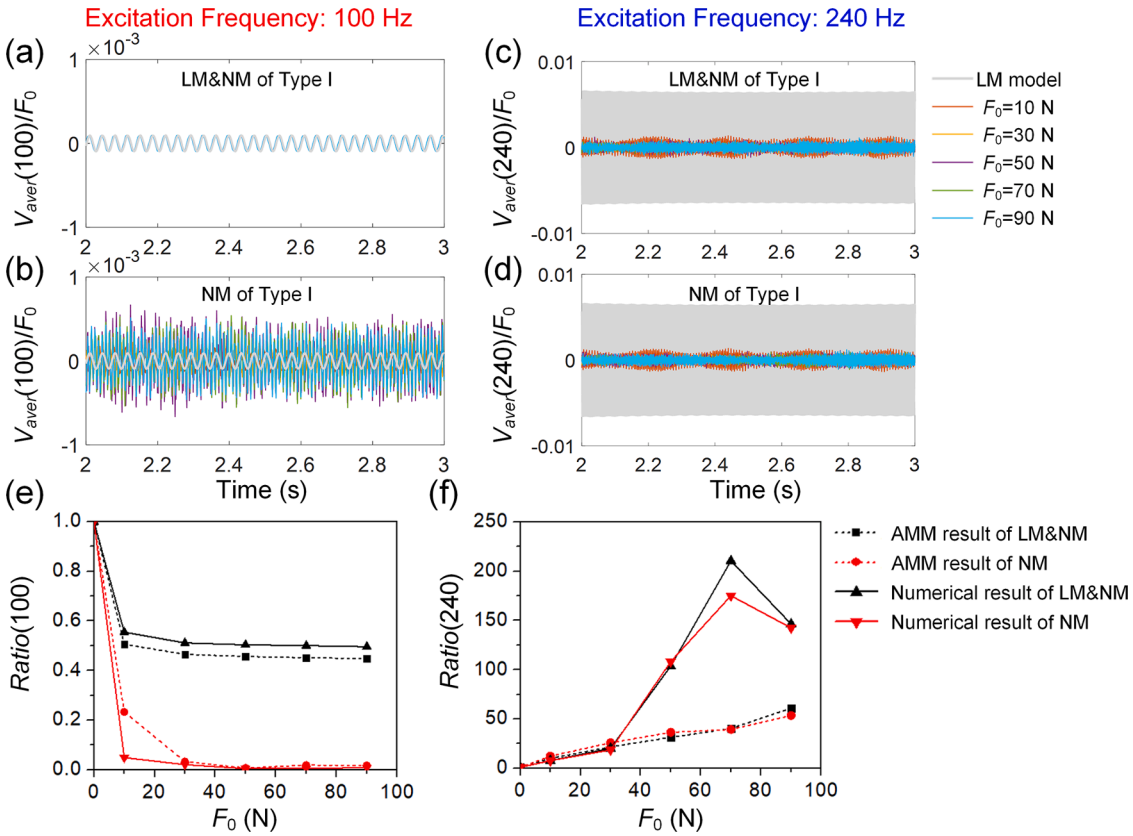

Fig. 4. Numerical reponses and its statistics datas obtained by time-domain simulation with increasing F_0. (a, c) Normlized average velocities of LM&NM. (b, d) Normlized average velocities of NM. (e, f) Comparisions of *Ratio* between the AMM and numerical methods. (a, b, e) $f = 100$ Hz; (c, d, f) $f = 240$ Hz.

they cannot build up deep vibration valleys. Most importantly, linear bandgaps produces consistent vibration valleys regardless of the excitation amplitudes. As shown in Fig. 3(b), integrating linear oscillators into the NM framework yields the LM&NM model, which preserves the vibration valley (blue region) under increasing F_0. This valley corresponds to the linear-resonator-induced bandgap. Simultaneously, the chaotic bands from nonlinear resonators suppress most passband peaks. At $F_0 = 90$ N as shown in Fig. 3(c), remarkable differences emerge between the two models: $Rb_{\min}$ of LM&NM dowells and persists at least 93 %, whereas that of NM can hardly exceed 76 % as shown in Fig. 3(d). Both models exhibit comparable passband suppression with Rp_{mean} increasing by around 8 dB as shown in Fig. 3(f). Thus, the LM&NM model provide more robust and consistent bandgap performance while enabling chaotic passband suppression.

Furthermore, time-domain simulations validate this characteristic, as shown in Fig. 4. At 100 Hz excitation (within the bandgap), LM&NM maintains normalized amplitudes below 1×10^{-4}, whereas NM exhibits amplitudes up to 6×10^{-4} as shown in Fig. 4 (a, b). This confirms LM&NM's capability to maintain bandgap performance under increasing nonlinearity. At 240 Hz (within the passband), both models display nearly identical normalized amplitudes that decrease with rising F_0 as shown in Fig. 4(c, d). Frequency spectra exhibit comparable vibration suppression characteristics (Fig. 4(e, f)), validating both models' passband vibration suppression efficacy. Collectively, these results demonstrate the unique ability of LM&NM to simultaneously maintain bandgap integrity and leverage chaotic passbands for broadband vibration reduction.

Therefore, design guidance for Type I systems can be summarized as follows:

1. For applications requiring exclusively resonance peak suppression only, the NM model is recommended.
2. When deep vibration valleys are the primary requirement, the LM model should be selected.
3. For scenarios demanding both deep vibration valleys and resonance peak supression, the LM&NM model is the optimal solution.

3.2. Experimental validation

To implement the LM&NM design and validate its numerically predicted performance, we conducte experimental verification. Achieving strong nonlinearity under moderate excitation amplitudes remains challenging in NAMs. Vibro-impact [18,28,33] provides a viable approach for realizing the required nonlinearity level. Previous comparative studies demonstrate similar dynamic properties between vibro-impact and cubic stiffness nonlinearities under weak and strong nonlinearity [29]. Consequently, we employ vibro-impact oscillators here to generate nonlinearity as shown in Fig. 5(a), enabling chaotic bands for passband vibration suppression.

In the vibro-impact oscillator, the primary mass m_{01} is a hollow parallelepiped rigidly connected to a thin plate by bolts. The sphere m_1, held inside m_{01}, is stuck to a cantilever beam whose radius is 10 mm. m_1 couples to m_{01} by this cantilever beam with a total stiffness k_1. A symmetrical clearance, $\delta = 50 \pm 20$ μm, is provisioned between the sphere m_1 and the wall m_{01}. When the relative displacement w_{1r} between them are larger than δ, nonlinear interaction takes place through m_1 colliding with m_{01}. As shown in Fig. 5(b), the linear oscillator counterpart uses identical parameters but has an enlarged clearance to prevent collision. The NAM meta-plate thickness is 0.003 m, with all other parameters matching the theoretical and simulation values. Simply-supported boundary conditions are approximated by clamping limited edge regions (orange area) as shown in Fig. 5(d). This minimal restraint area (small relative to the total plate area) provides weak constraint to boundary bending, thereby approximating simply-supported behavior. Other parameters are $m_0 = m_{01}+m_{02} = 70$ g, $m_1 = m_2 = 32$ g, $f_1 = f_2 = 280$ Hz.

As shown in Fig. 5(c, d), a signal generator (Tektronix, AFG1022X) supplies the input signal coded by a computer, to a power amplifier (Brüel&Kjær, Type 2706). The power amplifier boosts the input signal by 15 dB and drives the shaker (Brüel&Kjær, Type 4809). A Doppler Laser Vibrometer (Polytec, PSV-500) records the transient velocity of the plate and transmits the data to a computer for further processing. White-noise excitation at three voltage levels (1 V, 5 V, 9 V) produces progressively increasing nonlinear levels as shown in Fig. 6(b). Instead of direct force measurement, we use the transmission T defined as:

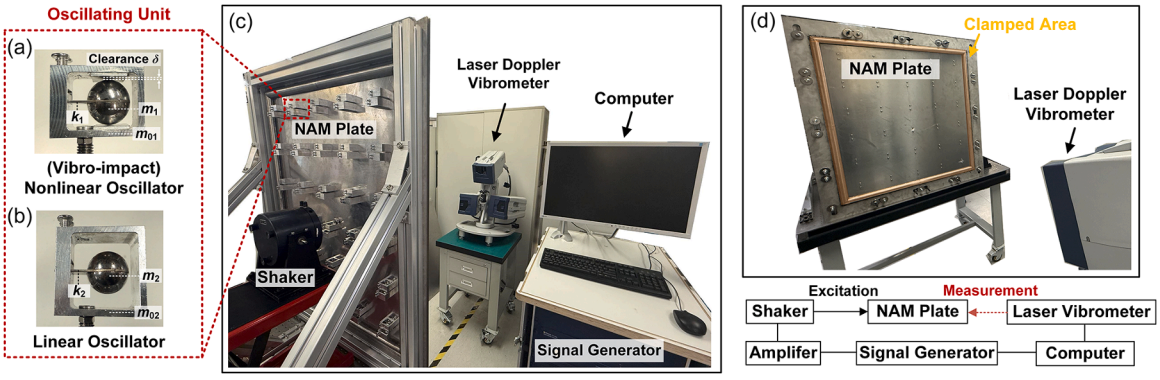

Fig. 5. Experimental setup. (a) Specimen of the vibro-impact nonlinear oscillator. (b) Specimen of the linear oscillator. (c) and (d) System for measuring the response of the meta-plate with oscillators of (a) and (b) from two perspectives.

$$T(f) = \frac{\sqrt{\sum_{i=1}^{30} (V_s(f))^2 S_s / S_{total}}}{V_0}, \tag{14}$$

$$RT(f) = 20\lg(T(f)). \tag{15}$$

The corresponding evaluation criteria for the bandgaps and passbands can be redefined according to Section 2.2:

$$RTb_{\min} = 20\lg(\min(\sum_{f=f_{\text{bandgap\_start}}}^{f_{\text{bandgap\_end}}} T(f))) \text{and } RTp_{\text{mean}} = 20\lg(\text{mean}(\sum_{f=f_{\text{passband\_start}}}^{f_{\text{passband\_end}}} T(f))), \tag{16}$$

where V_0 is the velocity of the excitation point.

Fig. 6(a) presents the simulated and experimentally measured transmission *RT*. Under low (e.g., 1 V) input, no vibro-impact collision occurs and the system exhibits linear behavior. Rayleigh damping and resonator damping parameters for the experimental model were deduced from a comparison of the transmissions depicted in Appendix. A.3. The mass proportional coefficient (α) and the stiffness proportional coefficient (β) were determined to be 34.27 and 7.23 × 10^{-7}, respectively. The damping coefficient of the resonators was set to $c_i = 0.01k_i/\omega_i$, $i = 1, 2$. The close alignment between the experimental and simulated peak frequencies validates the simply-supported boundary implementation. Minor bandgap discrepancies arise from oscillator resonance frequency variations (280 ± 5 Hz). Fig. 6(b) shows the *RT* evolution with input voltage escalation (1 V→9 V). Within the bandgap, transmission valleys show slight elevation; passband behavior diverges: pre-bandgap peaks remain stable while post-bandgap peaks attenuate, consistent with theoretical predictions. Statistical analysis in Fig. 6(b, c) confirms that $RTb_{\min}$ maintains at least 90 %, and the RTp_{mean} after the bandgap increase by 2 dB. The experimental results at 9 V input align with F_0 = 8 N simulation data, as shown in Fig. 3(d–f), collectively demonstrating successful bandgap preservation and passband vibration suppression features.

4. Type II system: effects of nonlinearity location, linear stiffness and damping

Type I system constitutes a configuration derived from a 1DoF oscillator nonlinear meta-plate in Section 3.1. Type II system extends this configuration by separating the two resonant frequencies of the oscillators from $f_1 = f_2$ to $f_1 \neq f_2$. To investigate this generalization, we adapt the stiffness k_2 to cope with the resonant frequencies f_2 = 150, 200, 250, 300, 350, 400 Hz, while keeping f_1 = 100 Hz constant, thus resulting in six distinct cases. Compared with Type I, Type II is more suitable for evaluating the effects of nonlinearity location, linear stiffness and damping. Furthermore, this system allows for understanding why nonlinearity preferentially suppresses post-bandgap rather than pre-bandgap passbands. These insights provide useful guidance for optimizing combinational design

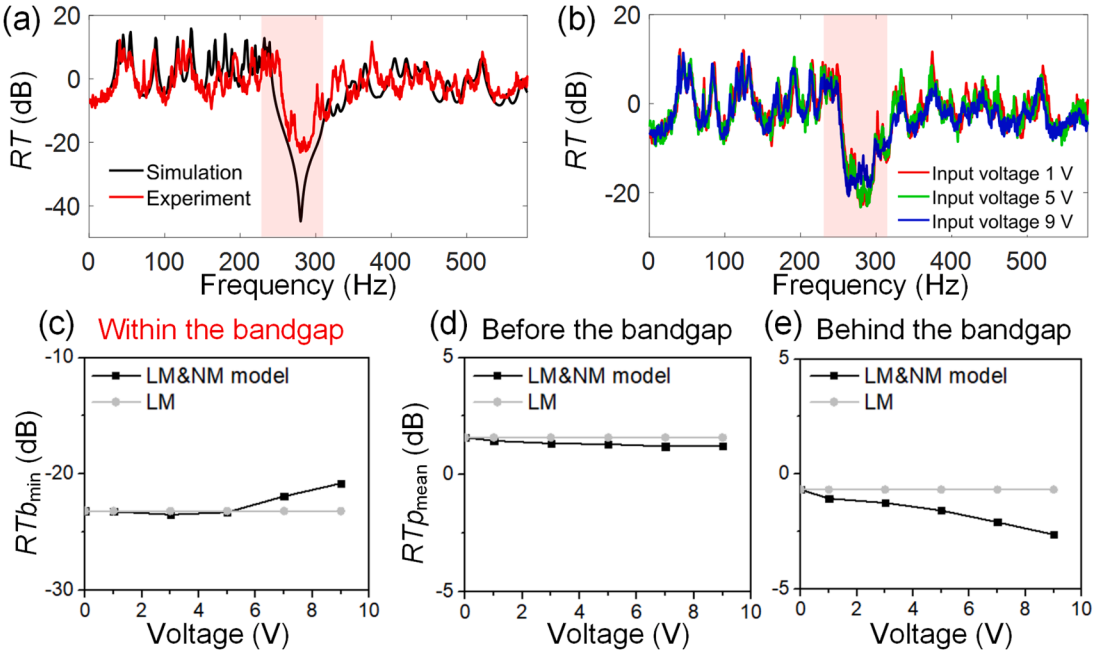

Fig. 6. Experimental transmissions and their statistics datas with increasing input voltage. (a) Comparison of *RT* for the linear meta-plate between simulation and experiment. (b) *RT* of the cominational design. (c-e) The trend of $RTb_{\min}$ and RTP_{mean} within the bandgap of (c); before the bandgap of (d); behind the bandgap of (e).

strategies. One may also treat Type I as a special case of Type II model with $f_1 = f_2$. All four design strategies (LM, LM&NM 1, LM&NM 2 and NM) are evaluated within this framework.

Fig. 7(a) presents a representative R for the NM model with $f_1 = 100$ Hz and $f_2 = 300$ Hz under increasing F_0. The spectra comprise five distinct regions: two bandgaps (the first and second) and three passbands (the first, second and third). For the two bandgaps, the first valley attenuates with increasing nonlinearity, while the second maintains its transmission valley. For the passbands, peak suppression intensifies progressively in the second and third passbands compared to the first. To systematically quantify these variations and elucidate their underlying mechanisms, we conduct a comparative analysis across all six cases using established evaluation criteria and examine the nonlinear phenomena sequentially.

4.1. Effect of nonlinearity location

As $Ratio\_Rb_{\min}$ and $Ratio\_Rp_{\text{mean}}$ are defined in Eq. (12), $Ratio\_Rb_{\min} < 1$ indicates that the minimum transmission within the bandgap exceeds that of the LM model, while $Ratio\_Rp_{\text{mean}} < 1$ signifies higher average passband transmission relative to the LM baseline.

The first bandgap, as shown in Fig. 7(b) disappear after introducing nonlinearity into k_1: $Ratio\_Rb_{\min}$ for all six cases fall below 10 %. Conversely, introducing nonlinearity into k_2 only affects the second bandgap as shown in Fig. 7(f) rather than the first as shown in Fig. 7(c). This is because the resonant frequencies are independently determined by the two oscillators in parallel. Therefore, introducing nonlinearity does not take into account the coupling of the two oscillators. Also, the two oscillators can also be connected in series (see Appendix A.5). However, the parallel configuration offers key advantages over the serial design. Its operational principle relies on the relatively independent motion of the two mass blocks, which helps maintain a complete bandgap. Additionally, the parallel configuration provides superior vibration suppression performance within the chaotic band.

4.2. Effect of linear stiffness

Interestingly, although introducing nonlinearity into k_2 can also affect the second bandgap, the $Ratio\_Rb_{\min}$ evolution under

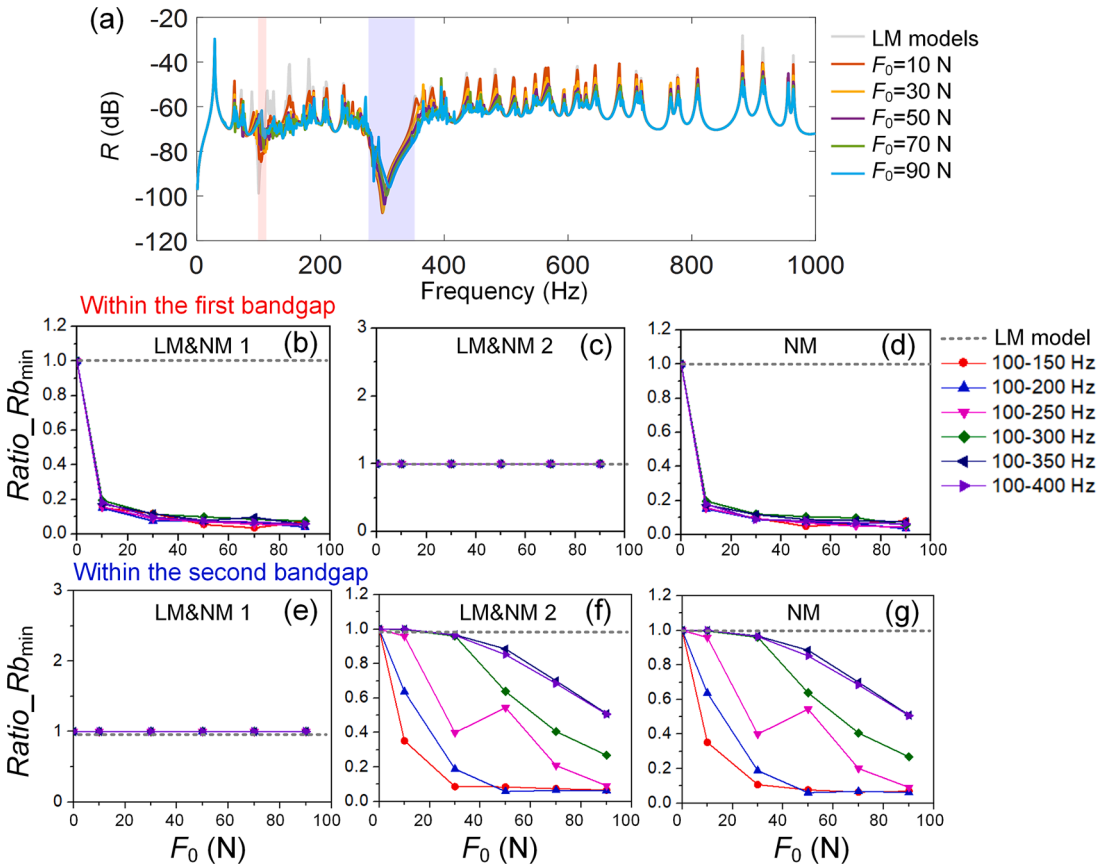

Fig. 7. Ananlytical responses and their bandgap statistics datas for the six cases with different resonance frequencies as F_0 increases. (a) R for NM when f_1=100 Hz and f_2=300 Hz. (b, c, d) $Ratio\_Rb_{\min}$ of the first bandgap. (e, f, g) $Ratio\_Rb_{\min}$ of the second bandgap. (b, e) are the results of LM&NM 1; (c, f) are the results of LM&NM 2; (d, g) are results of NM.

increasing F_0 exhibits distinct trends across the six frequency cases as shown in Fig. 7(f, g). As f_2 increases, the robustness of the nonlinear bandgap improves. We analyze this phenomenon through two representative LM&NM 2 cases: (1) $f_1 = 100$ Hz, $f_2 = 150$ Hz and (2) $f_1 = 100$ Hz, $f_2 = 400$ Hz, as shown in Fig. 8. Obviously, nonlinearity causes the disappearance of the second bandgap (blue area) for $f_2 = 150$ Hz but not for $f_2 = 400$ Hz, as shown in Fig. 8(a, b). When the resonance frequency f_2 is shifted to a higher frequency, the value of $k_2 = (2\pi f_2)^2 m_2$ increases. This causes the nonlinear interaction force F_r between m_2 and m_0 to approach linear behavior as shown in Fig. 8(d). Consequently, oscillators with higher stiffness exhibit reduced nonlinear sensitivity at the same excitation forces. Thus, it is necessary to consider whether the excitation force is sufficient to induce the required nonlinearity.

4.3. Effect to the passband after the bandgap

Notably, k_{1N} affects the second passband but not the first passband in all six cases, consistent with the observation made in Section 3.1: $Ratio\_Rp_{mean}$ of the six cases all increase within the second passband, as shown in Fig. 9 (d–f) while remaining almost stable within the first passband as shown in Fig. 9(a–c). Similarly, k_{2N} affects the third passband but not the second passband: $Ratio\_Rp_{mean}$ of the six cases all increase within the third passband as shown in Fig. 9(g–i) but remains almost unchanged within the second passband as shown in Fig. 7(e). Thus, introducing nonlinearity into the oscillators with a resonance frequency of f_x can suppress the passband after f_x. As explained in our work [24–26], the hardened NAM influences all passbands that are higher than the nonlinear LR bandgap.

To validate this phenomenon, time-domain simulations are conducted at an excitation frequency of 190 Hz (within the second passband) for the $f_1 = 100$ Hz and $f_2 = 300$ Hz configuration as shown in Fig. 10. As F_0 increases, $Ratio\_Rp_{mean}$ rises for both LM&NM 1 and NM, but remains stable for LM&NM 2. This confirms that vibration suppression at 190 Hz requires the presence of k_{1N}. These findings provide critical design guidance: to maximize chaotic band coverage for vibration suppression, nonlinear elements should be implemented in oscillators with the minimal feasible stiffness.

4.4. Effect of damping on nonlinear responses

Irrespective of the nonlinearity location, the third passband exhibits consistent vibration suppression evidenced by the increased $Ratio\_Rp_{meam}$ as shown in Fig. 9(g–i). However, a higher f_2 reduces the growth rate of $Ratio\_Rp_{meam}$, indicating impaired suppression efficacy. This attenuation stems from the concurrent increase in damping $c_2 = 0.01k_2/\omega_2$. Although this damping is minimal, it reduces the vibration after the second bandgap (Fig. 11(c)) and constrains the relative displacement w_{1r} between m_1 and m_0. This compromises the nonlinear effects, in the same way as discussed in Ref. [17,29]. Consequently, increasing damping impair the vibration suppression through chaotic band effects. As shown in Fig. 11(d, e), to highlight this phenomenon, we remove c_2, showing that the suppression effect in the third passband occurs without damping but becomes less effective with damping. Thus, damping-induced suppression of

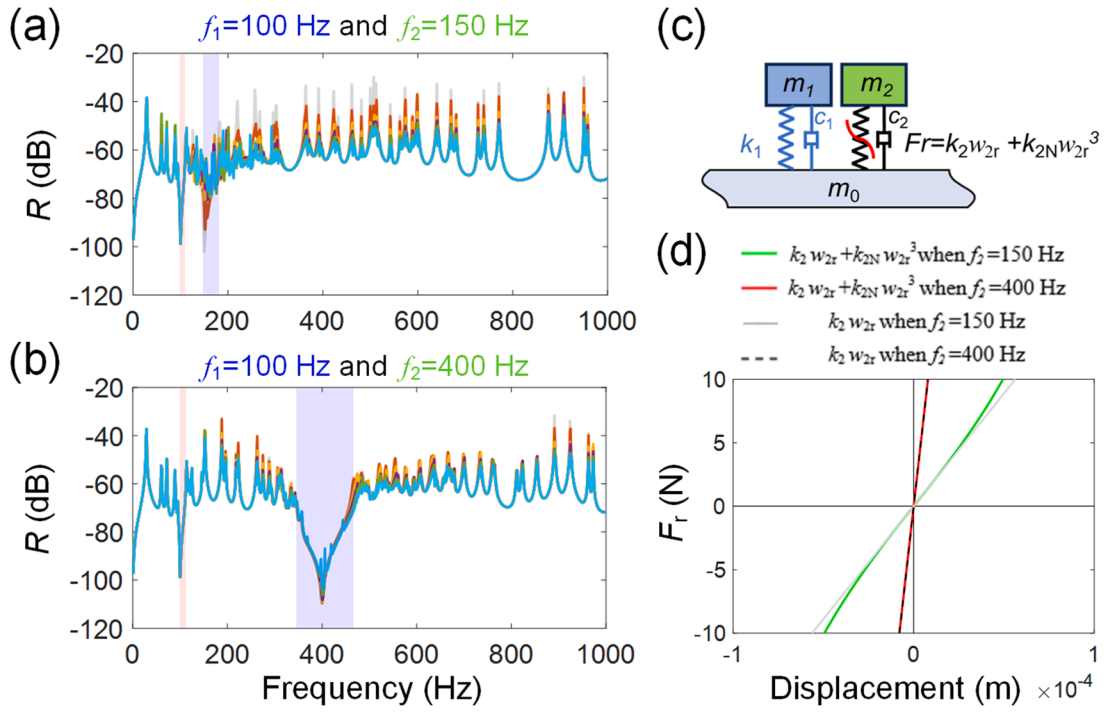

Fig. 8. Effect of nonlinear stiffness. (a) R for LM&MN 2 when $f_1 = 100$ Hz and $f_2 = 150$ Hz. (b) R for LM&MN 2 when $f_1 = 100$ Hz and $f_2 = 400$ Hz. (c) Single oscillator of LM&MN 2 (d) Relationships between F_r and w_{2r}.

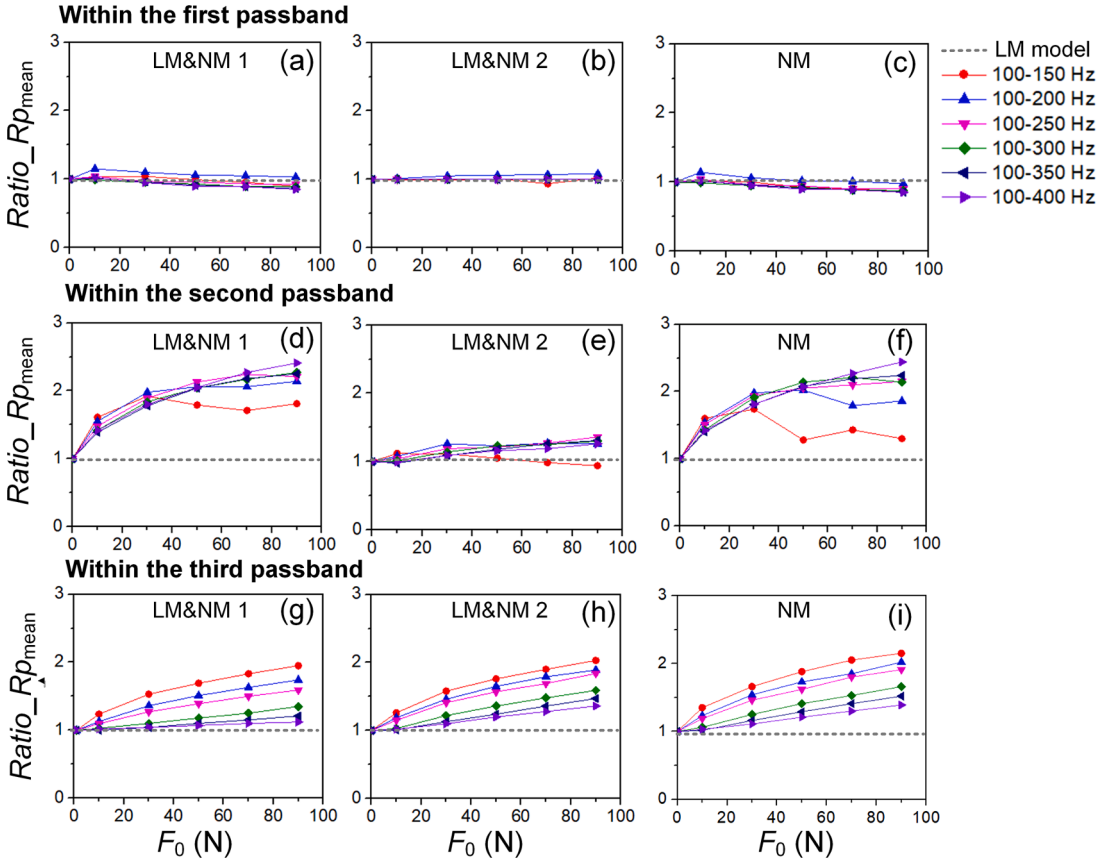

Fig. 9. Passband statistics datas for the six cases with different resonance frequencies as F_0 increases. (a, b, c) *Ratio_Rp*$_{mean}$ of the first passband. (d, e, f) *Ratio_Rp*$_{mean}$ of the second passband. (g, h, i) *Ratio_Rp*$_{mean}$ of the third passband. (a, d, g) are the results of LM&NM 1; (b, e, h) are the results of LM&NM 2; (c, f, i) are results of NM.

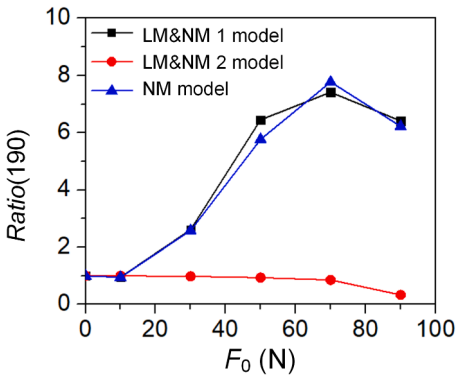

Fig. 10. Cmparsions of *Ratio_RP*$_{mean}$ among single oscillators: LM&NM 1, LM&NM 2 and NM.

nonlinear effects directly causes the observed *Ratio_Rp*$_{meam}$ growth rate reduction at higher f_2.

Guidence for designing Type II system can be summarised as follows:

1. The metacell resonant frequencies can be independently determined by parallel oscillators, eliminating the coupling considerations during nonlinearity implementation.
2. Oscillators with higher stiffness exhibit reduced nonlinear sensitivity at the same excitation force. Thus, it is necessary to consider whether the excitation force is sufficient to induce the required nonlinearity.

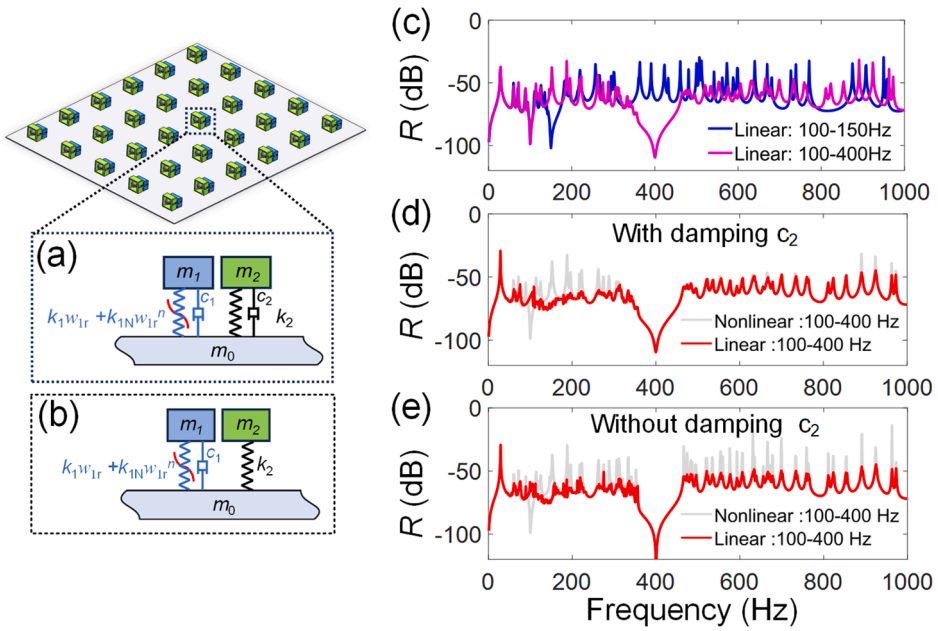

Fig. 11. Influence of damping on nonlinearity expression (a) LM&NM 1 model with damping c_1 and c_2. (b) LM&NM 1 model only with damping c_1. (c) R for LM model when $f_1 = 100$ Hz, $f_2 = 150$ Hz and $f_1 = 100$ Hz, $f_2 = 400$ Hz, respectively. (d) R for LM and LM&NM 1 models composed of (a). (e) R for LM and LM&NM 1 models composed of (b).

3. To maximize chaotic band coverage for vibration suppression, nonlinear elements should be implemented in oscillators with minimal feasible stiffness.
4. Reduced oscillator damping enhances the manifestation of the nonlinear effect in the meta-plate.

5. Conclusions

This work leverages the complementary benefits of both LAM and NAM to address the degeneration of the linear bandgap caused by nonlinearity, while preserving broadband vibration suppression in the chaotic band. The combined structure is implemented within a high-dimensional NAM system to experimentally demonstrate its effectiveness and to elucidate the underlying physical mechanisms. Two types of systems are investigated: Type I with equal bandgap frequencies $f_1 = f_2$ and Type II with different bandgap frequencies $f_1 \neq f_2$. By integrating the substantial bandgaps of the LAMs with the ultra-broadband suppression of the NAMs, Type I improves the vibration reduction in bandgap by 17 dB compared to traditional NAMs while maintaining a stable chaotic band with minimal fluctuation (3 dB). Its superior performance is experimentally validated using a configuration comprising vibro-impact and linear oscillators.

Type II represents a general case, with resonant frequencies f_1 and f_2 independently set to two parallel oscillators, enabling uncoupled frequency selection to meet specific requirements. In this type, we reveal the effects of the nonlinearity location, linear stiffness and damping on the suppression effect in different frequency ranges. The results provide guidance for combinational designs: Elevated stiffness and damping suppress nonlinear effects; thus, necessitating optimized stiffness and damping levels. Moreover, hardening nonlinearity generates chaotic bands primarily after the bandgap corresponding to the nonlinear resonator, thereby reducing post-resonance responses. To maximize the vibration suppression, nonlinear elements should be implemented in oscillators with minimal and feasible stiffness. Leveraging these insights, the proposed design achieves a significant extension of broadband vibration suppression into lower frequency ranges, accompanied by a notable improvement in its overall effectiveness.

Based on this work, we believe the proposed design is expected to contribute not only to vibration control but also potentially to sound radiation control. The proposed technique may lead to better and broader-band noise suppression effects than their linear counterparts, which would have economic benefits in areas such as naval vessel stealth, energy saving, and precision manufacturing. However, in terms of acoustics, attention should be paid to the contribution of nonlinear higher harmonics, as an increase in frequency implies enhanced sound radiation efficiency. The influence of nonlinearity on sound radiation requires further investigation.

CRediT authorship contribution statement

Chen Gong: Writing – review & editing, Writing – original draft, Validation, Software, Methodology, Investigation, Formal analysis, Data curation, Conceptualization. **Xin Fang:** Writing – review & editing, Supervision, Resources, Project administration, Methodology, Funding acquisition, Formal analysis, Conceptualization. **Hangxing Li:** Writing – review & editing, Validation. **Zhiyuan Li:** Writing – review & editing, Validation. **Li Cheng:** Writing – review & editing, Supervision, Resources, Project administration, Methodology, Funding acquisition, Formal analysis, Conceptualization.

Declaration of competing interest

The authors declare that they have no known competing financial interests or personal relationships that could have appeared to influence the work reported in this paper.

Acknowledgements

This research was funded by the Research Grant Council of the Hong Kong SAR. Xin Fang is supported by the National Natural Science Foundation of China (Projects No. 52241103 and No. 52322505) and Natural Science Fund of Hunan Province (Project No. 2023JJ10055).

Appendix A.1. Specific expressions

Specific expression of Eq. (6) write:

$$
\begin{cases}
\displaystyle\int\!\!\int_{plate} \rho h \phi_{pq}(x,y)\phi_{pq}(x,y)\ddot{q}_{pq}(t)dxdy + \int\!\!\int_{plate} D\phi_{pq}(x,y)\left(\frac{\partial^4\phi_{pq}(x,y)}{\partial x^4} + 2\frac{\partial^4\phi_{pq}(x,y)}{\partial x^2 y^2} + \frac{\partial^4\phi_{pq}(x,y)}{\partial y^4}\right)q_{pq}(t)dxdy \\
= -\phi_{pq}(x_1,y_1)F_1(x_1,y_1) - \phi_{pq}(x_2,y_2)F_1(x_2,y_2) - \ldots - \phi_{pq}(x_{30},y_{30})F_1(x_{30},y_{30}) + \phi_{pq}(x_c,y_c)F_0(x_c,y_c)\sin(2\pi ft) \\
m_0\sum_{i=1}^{m_c}\sum_{j=1}^{n_c}\phi_{ij}(x_1,y_1)\ddot{q}_{ij}(t) - c_1\dot{w}_{1r}^1 - k_1w_{1r}^1 - k_{1N}\left(w_{1r}^1\right)^3 - c_2\dot{w}_{2r}^1 - k_2w_{2r}^1 - k_{2N}\left(w_{2r}^1\right)^3 = F_1(x_1,y_1) \\
m_1\left(\sum_{i=1}^{m_c}\sum_{j=1}^{n_c}\phi_{ij}(x_1,y_1)\ddot{q}_{ij}(t) + \ddot{w}_{1r}^1\right) + c_1\dot{w}_{1r}^1 + k_1w_{1r}^1 + k_{1N}\left(w_{1r}^1\right)^3 = 0 \\
m_2\left(\sum_{i=1}^{m_c}\sum_{j=1}^{n_c}\phi_{ij}(x_1,y_1)\ddot{q}_{ij}(t) + \ddot{w}_{2r}^1\right) + c_2\dot{w}_{2r}^1 + k_2w_{2r}^1 + k_{2N}\left(w_{2r}^1\right)^3 = 0 \\
\ldots \\
m_0\sum_{i=1}^{m_c}\sum_{j=1}^{n_c}\phi_{ij}(x_{30},y_{30})\ddot{q}_{ij}(t) - c_1\dot{w}_{1r}^{30} - k_1w_{1r}^{30} - k_{1N}\left(w_{1r}^{30}\right)^3 - c_2\dot{w}_{2r}^{30} - k_2w_{2r}^{30} - k_{2N}\left(w_{2r}^{30}\right)^3 = F_{30}(x_{30},y_{30}) \\
m_1\left(\sum_{i=1}^{m_c}\sum_{j=1}^{n_c}\phi_{ij}(x_{30},y_{30})\ddot{q}_{ij}(t) + \ddot{w}_{1r}^{30}\right) + c_1\dot{w}_{1r}^{30} + k_1w_{1r}^{30} + k_{1N}\left(w_{1r}^{30}\right)^3 = 0 \\
m_2\left(\sum_{i=1}^{m_c}\sum_{j=1}^{n_c}\phi_{ij}(x_{30},y_{30})\ddot{q}_{ij}(t) + \ddot{w}_{2r}^{30}\right) + c_2\dot{w}_{2r}^{30} + k_2w_{2r}^{30} + k_{2N}\left(w_{2r}^{30}\right)^3 = 0
\end{cases}
\tag{A1}
$$

Expressions of $\mathbf{A}_1$, $\mathbf{B}_1$, $\mathbf{C}_1$, $\mathbf{D}_1$, $\mathbf{E}_1$ and $\mathbf{F}_1$ write

$\mathbf{A}_1 = [A_1q_{11}, A_1q_{12},\ldots, A_1q_{mcnc}, A_1w_{1r}^1, A_1w_{2r}^1,\ldots, A_1w_{1r}^{30}, A_1w_{2r}^{30}]^T$; $\mathbf{B}_1 = [B_1q_{11}, B_1q_{12},\ldots, B_1q_{mcnc}, B_1w_{1r}^1, B_1w_{2r}^1,\ldots, B_1w_{1r}^{30}, B_1w_{2r}^{30}]^T$; $\mathbf{C}_1 = [C_1q_{11}, C_1q_{12},\ldots, C_1q_{mcnc}, C_1w_{1r}^1, C_1w_{2r}^1,\ldots, C_1w_{1r}^{30}, C_1w_{2r}^{30}]^T$; $\mathbf{D}_1 = [D_1q_{11}, D_1q_{12},\ldots, D_1q_{mcnc}, D_1w_{1r}^1, D_1w_{2r}^1,\ldots, D_1w_{1r}^{30}, D_1w_{2r}^{30}]^T$; $\mathbf{E}_1 = [E_1q_{11}, E_1q_{12},\ldots, E_1q_{mcnc}, E_1w_{1r}^1, E_1w_{2r}^1,\ldots, E_1w_{1r}^{30}, E_1w_{2r}^{30}]^T$; $\mathbf{F}_1 = [F_1q_{11}, F_1q_{12},\ldots, F_1q_{mcnc}, F_1w_{1r}^1, F_1w_{2r}^1,\ldots, F_1w_{1r}^{30}, F_1w_{2r}^{30}]^T$.

Expressions of $\boldsymbol{\alpha}_1$, $\boldsymbol{\alpha}_2$, $\boldsymbol{\alpha}_3$, $\boldsymbol{\alpha}_4$, $\boldsymbol{\alpha}_5$ and $\boldsymbol{\alpha}_6$ are

$$
\begin{cases}
\alpha_1 = 0.75\left(\mathbf{A}_1{}^3 + \mathbf{A}_1\mathbf{B}_1{}^2 - \mathbf{A}_1{}^2\mathbf{C}_1 + \mathbf{B}_1{}^2\mathbf{C}_1 + 2\mathbf{A}_1\mathbf{C}_1{}^2 - 2\mathbf{A}_1\mathbf{B}_1\mathbf{D}_1 + 2\mathbf{A}_1\mathbf{D}_1{}^2 + 2\mathbf{A}_1\mathbf{E}_1{}^2 + 2\mathbf{A}_1\mathbf{F}_1{}^2\right) \\
\alpha_2 = 0.75\left(\mathbf{A}_1{}^2\mathbf{B}_1 + \mathbf{B}_1{}^3 + 2\mathbf{A}_1\mathbf{B}_1\mathbf{C}_1 + 2\mathbf{B}_1\mathbf{C}_1{}^2 - \mathbf{A}_1{}^2\mathbf{D}_1 + \mathbf{B}_1{}^2\mathbf{D}_1 + 2\mathbf{B}_1\mathbf{D}_1{}^2 + 2\mathbf{B}_1\mathbf{E}_1{}^2 + 2\mathbf{B}_1\mathbf{F}_1{}^2\right) \\
\alpha_3 = 0.75\left(-\frac{1}{3}\mathbf{A}_1{}^3 + \mathbf{A}_1\mathbf{B}_1{}^2 + 2\mathbf{A}_1{}^2\mathbf{C}_1 + 2\mathbf{B}_1{}^2\mathbf{C}_1 + \mathbf{C}_1{}^3 + \mathbf{C}_1\mathbf{D}_1{}^2 - \mathbf{C}_1{}^2\mathbf{E}_1 + \mathbf{D}_1{}^2\mathbf{E}_1 + 2\mathbf{C}_1\mathbf{E}_1{}^2 - 2\mathbf{C}_1\mathbf{D}_1\mathbf{F}_1 + 2\mathbf{C}_1\mathbf{F}_1{}^2\right) \\
\alpha_4 = 0.75\left(-\mathbf{A}_1{}^2\mathbf{B}_1 + \frac{1}{3}\mathbf{B}_1{}^3 + 2\mathbf{A}_1{}^2\mathbf{D}_1 + 2\mathbf{B}_1{}^2\mathbf{D}_1 + \mathbf{C}_1{}^2\mathbf{D}_1 + \mathbf{D}_1{}^3 + 2\mathbf{C}_1\mathbf{D}_1\mathbf{E}_1 + 2\mathbf{D}_1\mathbf{E}_1{}^2 - \mathbf{C}_1{}^2\mathbf{F}_1 + \mathbf{D}_1{}^2\mathbf{F}_1 + 2\mathbf{D}_1\mathbf{F}_1{}^2\right) \\
\alpha_5 = 0.75\left(-\frac{1}{3}\mathbf{C}_1{}^3 + \mathbf{C}_1\mathbf{D}_1{}^2 + 2\mathbf{A}_1{}^2\mathbf{E}_1 + 2\mathbf{B}_1{}^2\mathbf{E}_1 + 2\mathbf{C}_1{}^2\mathbf{E}_1 + 2\mathbf{D}_1{}^2\mathbf{E}_1 + \mathbf{E}_1{}^3 + \mathbf{E}_1\mathbf{F}_1{}^2\right) \\
\alpha_6 = 0.75\left(-\mathbf{C}_1{}^2\mathbf{D}_1 + \frac{1}{3}\mathbf{D}_1{}^3 + 2\mathbf{A}_1{}^2\mathbf{F}_1 + 2\mathbf{B}_1{}^2\mathbf{F}_1 + 2\mathbf{C}_1{}^2\mathbf{F}_1 + 2\mathbf{D}_1{}^2\mathbf{F}_1 + \mathbf{E}_1{}^2\mathbf{F}_1 + \mathbf{F}_1{}^3\right)
\end{cases}. \tag{A2}
$$

Appendix A.2. Detailed description of sampling points amount and convergence analysis

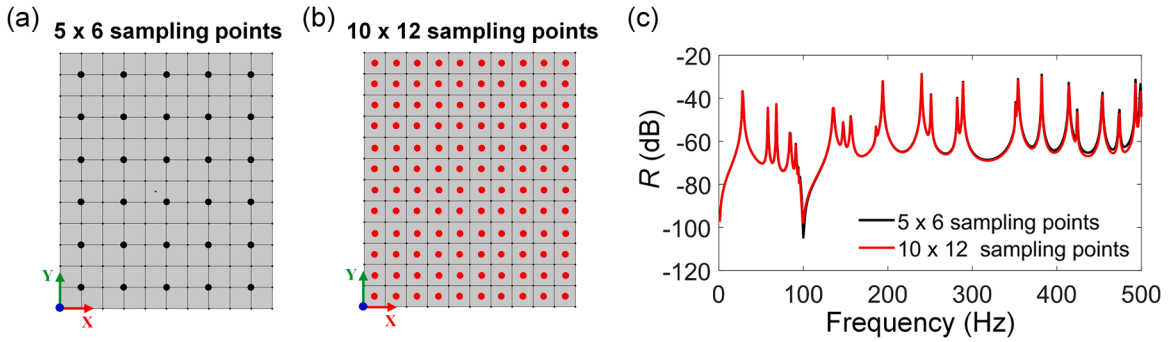

Fig. A1. Distribution of sampling points and convergence analysis. (a) 5 × 6 sampling points; (b) 10 × 12 sampling points; (c) *R* of (a) and (b).

To better capture the overall vibration level of the meta-plate, representative sampling points can be selected to calculate the parameter *R* according to Eqs. (9) and (10). Fig. A1 illustrates two different sampling point distributions and their corresponding *R* values. The results from both distributions show only minimal discrepancies: the peak frequencies align exactly, with slight deviations occurring at a few peak and valley locations. This is understandable, since within the frequency range of interest, the structural wavelength is rather long so that the 5 × 6 spatial sampling scheme, is already enough. Given the negligible difference in accuracy and the reduced computational cost, the 5 × 6 sampling scheme—which uses fewer points—was selected as an acceptable trade-off between computational efficiency and result fidelity.

Appendix A.3. Detailed description of FEM

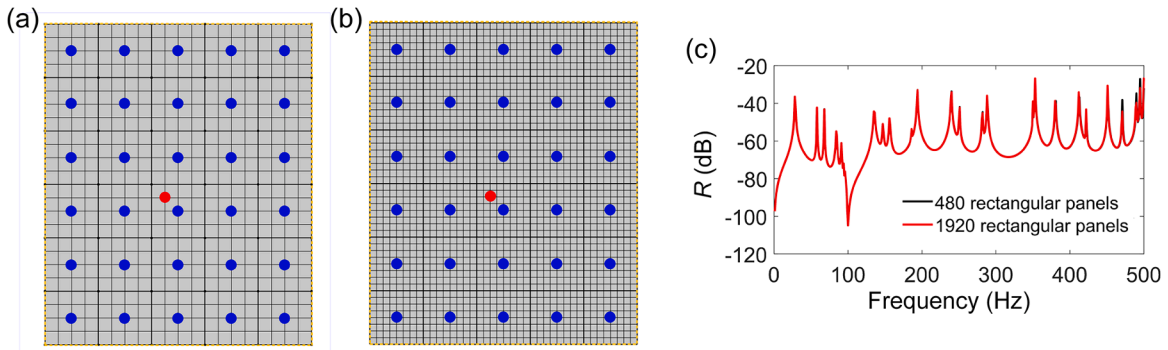

Fig. A2. Finite element mesh generation and convergence analysis. (a) 480 rectangular units and 30 metacells; (b) 1920 rectangular units and 30 metacells; (c) *R* of (a) and (b).

Based on the finite element method and the Kirchhoff–Love plate theory [51,52], we model the 2D meta-plate as shown in Fig. A2, with 30 metacells (blue points). A convergence analysis was conducted on the number of finite elements to be used. As shown in Fig. A2 (a, b), the units are discretized into 480 and 1920 rectangular plates, respectively. Fig. A2(c) shows that the two sets of results in terms of R exhibit minimal discrepancy between the two discretization schemes: Peak frequency deviations are $\leq$1 %. Accordingly, the former discretization with the fewer elements was selected, as an acceptable compromise between the computational time and accuracy of the results. The specific finite element modelling method is detailed in our work [14].

Appendix A.4. Damping of the experimental model

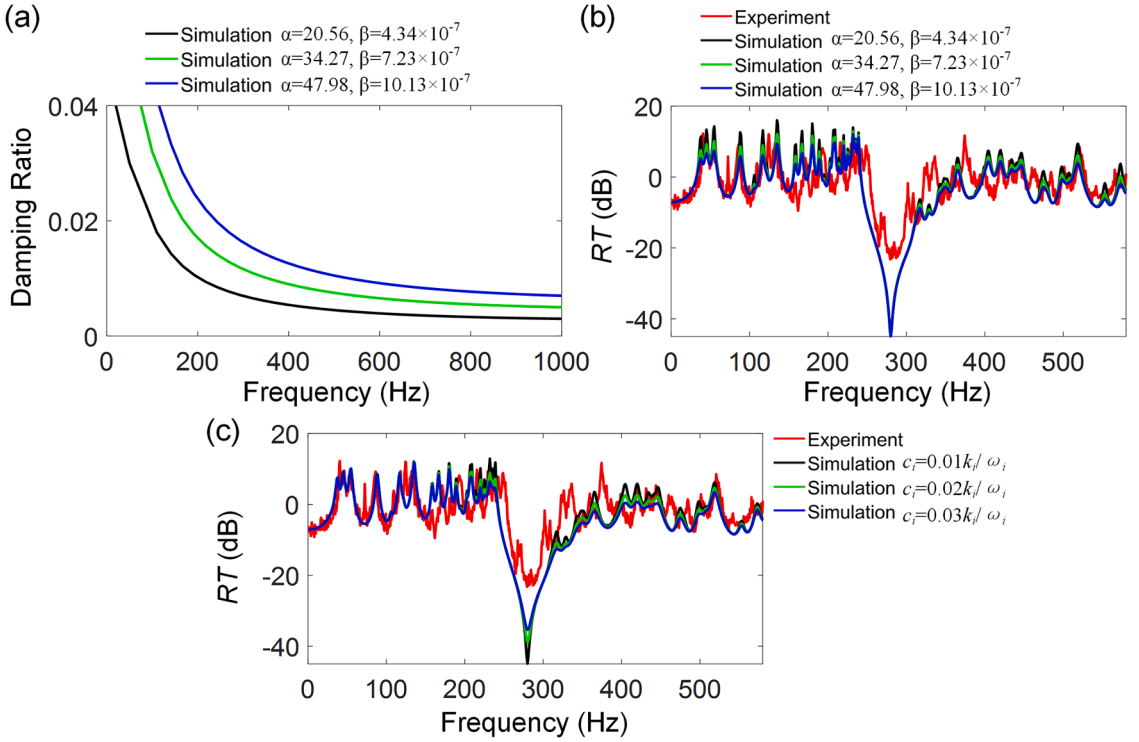

Fig. A3. Damping of the experimental model. (a) Rayleigh Damping ratio of the plate; (b) Transmission in varying Rayleigh damping when $c_i = 0.02k_i/\omega_i$, $i = 1, 2$; (c) Transmission in varying oscillator damping when $\alpha = 34.27$ and $\beta = 7.23 \times 10^{-7}$.

The damping in the experimental model mainly arises from two sources: the damping inherent in the plate, which is characterized by Rayleigh damping model as illustrated in Fig. A3(a), and the damping associated with the oscillators. To quantify the specific contributions of these two forms of damping, we examined their individual impacts on the transmission (RT). When the damping of the oscillator is held constant, variations in Rayleigh damping affect all the peaks, as shown in Fig. A3(b). Conversely, when Rayleigh damping is fixed, the damping of the oscillator influences the peaks and valleys near and beyond the bandgap, also demonstrated in Fig. A3(b). Therefore, the calibration procedure consists in first adjusting the Rayleigh damping to achieve consistency in the response before the bandgap, and then fine-tuning the oscillator damping to ensure agreement around and beyond the bandgap. Accordingly, the mass proportional coefficient (α) and the stiffness proportional coefficient (β) were initially determined to be 34.27 and 7.23×10^{-7}, respectively. Following this, the damping coefficient of the resonators was set to $c_i = 0.01k_i/\omega_i$, $i = 1, 2$.

Appendix A.5. Vibration responses in series and parallel models

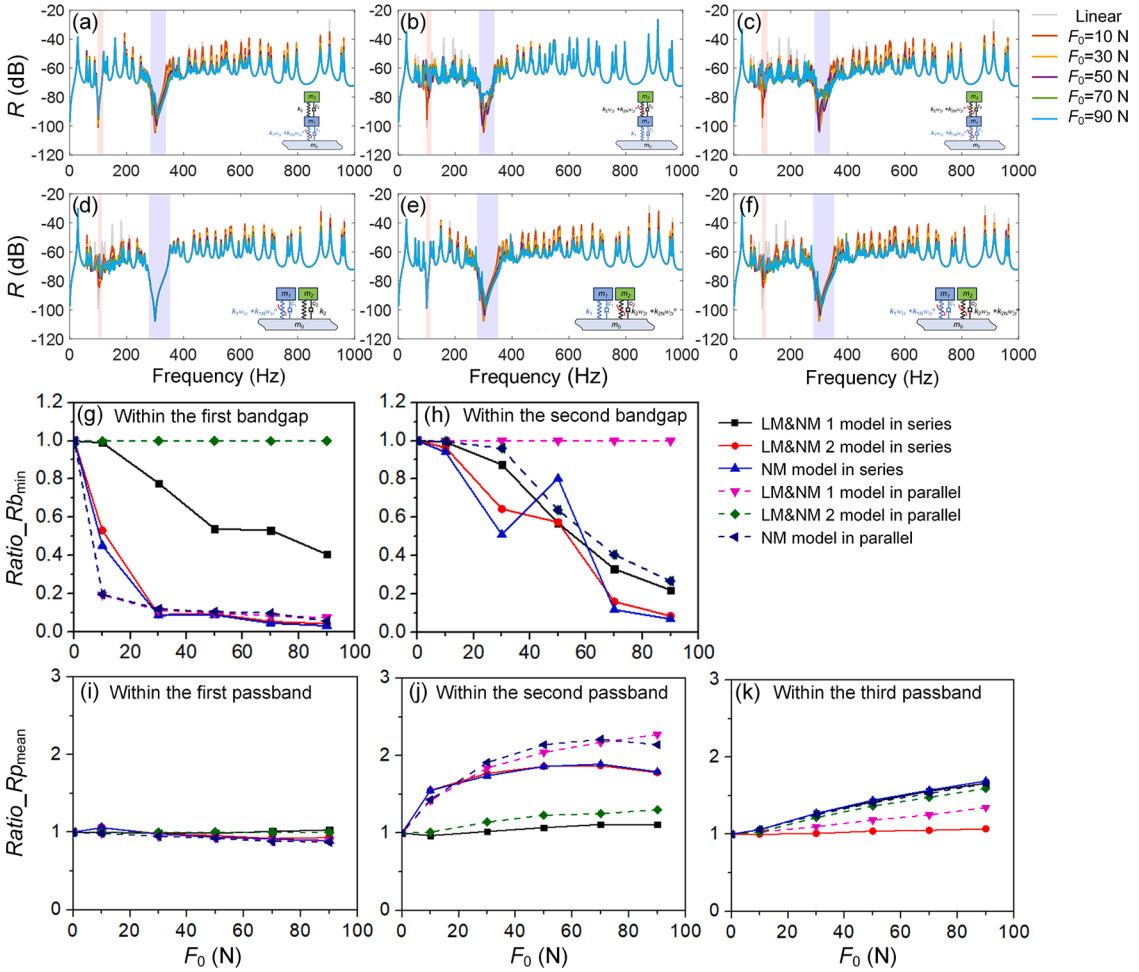

Fig. A4. Calculated results and their statistics datas for the meta-plate with oscillators in series and parallel when $f_1 = 100$ Hz and $f_2 = 300$ Hz as F_0 increases. R for the series models of (a-c); for the parallel models of (d-f). (a, d) LM&NM 1 model; (b, e) LM&NM 2 model; (c, f) NM model. (g, h) $Ratio\_Rb_{\min}$ of the first and second bandgap, respectively. (i, j, k) $Ratio\_Rp_{\text{mean}}$ of the first, second and third passband, respectively.

Fig. A4 shows the R of the nonlinear meta-plate with oscillators in series and parallel when $f_1 = 100$ Hz and $f_2 = 300$ Hz. We take this expample to demonstrate the difference between the series and parallel combination. Within the bandgaps shown in Fig. A2(g, h), bandgaps in series models all disappear as the level of nonlinearity increases, while LM&NM 1 and LM&NM 2 models in parallel can maintain the first and the second bandgap, respectively. This difference can be attributed to the resonance mechanisms. The resonance of a parallel oscillator is caused by the rather independent motion of the two masses, whereas the resonance of a series oscillator is caused by the coupled motion of the two masses. Therefore, introducing nonlinearity into a series oscillator with two masses alters the designed resonant frequencies of the two oscilattors before they are put into series, thereby affecting the two bandgaps as the same time. Furthermore, this also induces different changes in the chaotic bands as the nonlinearity increases. For instance, within the passbands as shown in Fig. A4(i–k), LM&NM 1 model in series shows almost the same R with that of LM&NM 2 model in parallel in Fig. A4(d).

According to the statistical data of Fig. A4(g–k), the series models offer additional options for meeting specific vibration suppression requirements. For example, LM&NM 1 model in series can be selected to maintain good bandgap effect while suppressing vibration in the passband. Although neither bandgap can maintain a complete bandgap, both show a greater $Ratio\_Rb_{\min}$ than most other options.

In summary, the parallel configuration offers distinct design advantages over the serial configuration. The primary advantage stems from the operational principle of the parallel oscillators, whose resonances arise from the relatively independent motion of two mass blocks. This inherent characteristic enables the preservation of a complete bandgap. Furthermore, the parallel configuration offers superior vibration reduction within the chaotic band. A comparative analysis reveals that: within the first passband, both configurations exhibits comparable performance; within the second passband, the parallel LM&NM1 and NM configurations demonstrate outstanding effectiveness; within the third passband, the serial LM&NM1 and NM configurations, alongside the parallel LM&NM2 configuration, show exceptional performance.

Data availability

The majority data has been shown in this paper. All data for this study, if not included in this published article, are available from the corresponding author on reasonable request.

References

[1] N. Gao, et al., Acoustic metamaterials for noise reduction: a review, Adv. Mater. Technol. 7 (2022) 2100698.
[2] J. Liu, H. Guo, T. Wang, A review of acoustic metamaterials and phononic crystals, Crystals 10 (2020) 305.
[3] M.-H. Lu, L. Feng, Y.-F. Chen, Phononic crystals and acoustic metamaterials, Mater. Today 12 (2009) 34–42.
[4] G. Ma, P. Sheng, Acoustic metamaterials: from local resonances to broad horizons, Sci. Adv. 2 (2016) e1501595.
[5] Z. Tao, et al., A novel auxetic acoustic metamaterial plate with tunable bandgap, Int. J. Mech. Sci. 226 (2022) 107414.
[6] X. Fang, W. Lacarbonara, L. Cheng, Advances in nonlinear acoustic/elastic metamaterials and metastructures, Nonlinear Dyn. (2024) 1–28.
[7] M.D. Fronk, L. Fang, P. Packo, M.J. Leamy, Elastic wave propagation in weakly nonlinear media and metamaterials: a review of recent developments, Nonlinear Dyn. 111 (2023) 10709–10741.
[8] B. Hu, X. Fang, J. Wen, D. Yu, Effectively reduce transient vibration of 2D wing with bi-stable metamaterial, Int. J. Mech. Sci. 272 (2024) 109172.
[9] Y. Shen, W. Lacarbonara, Wave propagation and multi-stopband behavior of metamaterial lattices with nonlinear locally resonant membranes, Int. J. Non Linear Mech. 161 (2024) 104671.
[10] C. Cai, et al., Flexural wave attenuation by metamaterial beam with compliant quasi-zero-stiffness resonators, Mech. Syst. Signal Process. 174 (2022) 109119.
[11] K. Wang, J. Zhou, Q. Wang, H. Ouyang, D. Xu, Low-frequency band gaps in a metamaterial rod by negative-stiffness mechanisms: design and experimental validation, Appl. Phys. Lett. 114 (2019).
[12] C. Zhao, K. Zhang, P. Zhao, Z. Deng, Finite-amplitude nonlinear waves in inertial amplification metamaterials: theoretical and numerical analyses, J. Sound Vib. 560 (2023) 117802.
[13] C. Gong, X. Fang, L. Cheng, Band evolution and 2D nonreciprocal wave propagation in strongly nonlinear meta-plates, Nonlinear Dyn. (2024) 1–21.
[14] X. Fang, J. Wen, L. Cheng, B. Li, Bidirectional elastic diode with frequency-preserved nonreciprocity, Phys. Rev. Appl. 15 (2021) 054022.
[15] X. Fang, et al., Breaking the mass law for broadband sound insulation through strongly nonlinear interactions, New J. Phys. 25 (2023) 093010.
[16] X. Fang, J. Wen, B. Bonello, J. Yin, D. Yu, Ultra-low and ultra-broad-band nonlinear acoustic metamaterials, Nat. Commun. 8 (2017) 1288.
[17] X. Fang, P. Sheng, J. Wen, W. Chen, L. Cheng, A nonlinear metamaterial plate for suppressing vibration and sound radiation, Int. J. Mech. Sci. 228 (2022) 107473.
[18] P. Sheng, X. Fang, L. Dai, D. Yu, J. Wen, Synthetical vibration reduction of the nonlinear acoustic metamaterial honeycomb sandwich plate, Mech. Syst. Signal Process. 185 (2023) 109774.
[19] P. Sheng, X. Fang, D. Yu, J. Wen, Nonlinear metamaterial enabled aeroelastic vibration reduction of a supersonic cantilever wing plate, Appl. Math. Mech. 45 (2024) 1749–1772.
[20] P. Sheng, X. Fang, D. Yu, J. Wen, Mitigating aeroelastic vibration of strongly nonlinear metamaterial supersonic wings under high temperature, Nonlinear Dyn. (2024) 1–21.
[21] T. Li, X. Fang, J. Wen, Significantly broaden sound insulation of metamaterial plate via strongly nonlinear interaction, Nonlinear Dyn. (2025) 1–16.
[22] T. Li, et al., Integrated adjustable acoustic metacage for multi-frequency noise reduction, Appl. Acoust. 217 (2024) 109841.
[23] D.C. Brooke, O. Umnova, P. Leclaire, T. Dupont, Acoustic metamaterial for low frequency sound absorption in linear and nonlinear regimes, J. Sound Vib. 485 (2020) 115585.
[24] X. Fang, J. Wen, B. Bonello, J. Yin, D. Yu, Wave propagation in one-dimensional nonlinear acoustic metamaterials, New J. Phys. 19 (2017) 053007.
[25] X. Fang, J. Wen, J. Yin, D. Yu, Y. Xiao, Broadband and tunable one-dimensional strongly nonlinear acoustic metamaterials: theoretical study, Phys. Rev. E 94 (2016) 052206.
[26] X. Fang, J. Wen, J. Yin, D. Yu, Wave propagation in nonlinear metamaterial multi-atomic chains based on homotopy method, AIP Adv. 6 (2016).
[27] P. Sheng, X. Fang, J. Wen, D. Yu, Vibration properties and optimized design of a nonlinear acoustic metamaterial beam, J. Sound Vib. 492 (2021) 115739.
[28] X. Fang, J. Wen, H. Benisty, D. Yu, Ultrabroad acoustical limiting in nonlinear metamaterials due to adaptive-broadening band-gap effect, Phys. Rev. B 101 (2020) 104304.
[29] C. Gong, X. Fang, L. Cheng, Multi-state dynamics and model similarity of a vibro-impact nonlinear system, Int. J. Non Linear Mech. 163 (2024) 104765.
[30] X. Fang, J. Wen, D. Yu, J. Yin, Bridging-coupling band gaps in nonlinear acoustic metamaterials, Phys. Rev. Appl. 10 (2018) 054049.
[31] W. Tian, Z. Yang, M. Li, Y. Gu, T. Zhao, Theoretical modeling and mechanism analysis of nonlinear metastructure for supersonic aeroelastic suppression, Mech. Syst. Signal Process. 224 (2025) 111931.
[32] W. Tian, T. Zhao, Z. Yang, Supersonic meta-plate with tunable-stiffness nonlinear oscillators for nonlinear flutter suppression, Int. J. Mech. Sci. 229 (2022) 107533.
[33] M. Yu, X. Fang, J. Wen, D. Yu, Robust nonlinear elastic metamaterial enabled by collision damping, Mech. Adv. Mater. Struct. 31 (2024) 3630–3637.
[34] M. Yu, X. Fang, D. Yu, J. Wen, L. Cheng, Collision enhanced hyper-damping in nonlinear elastic metamaterial, Chin. Phys. B 31 (2022) 064303.
[35] J. Zhao, H. Zhou, K. Yi, I. Kovacic, R. Zhu, Ultra-broad bandgap induced by hybrid hardening and softening nonlinearity in metastructure, Nonlinear Dyn. 111 (2023) 17687–17707.
[36] B. Hu, X. Fang, L. Cheng, J. Wen, D. Yu, Attenuation of impact waves in a nonlinear acoustic metamaterial beam, Nonlinear Dyn. 111 (2023) 15801–15816.
[37] L. Xiao, X. Sun, L. Cheng, X. Yu, Broadband and robust vibration reduction in lattice-core sandwich beam with 3D-printed QZS resonators, Compos. Struct. 352 (2025) 118626.
[38] B. Zhao, et al., A nonlinear damped metamaterial: wideband attenuation with nonlinear bandgap and modal dissipation, Mech. Syst. Signal Process. 208 (2024) 111079.
[39] L. Xiao, M. Iqbal, X. Yu, Quasi-static band gaps in metamaterial pipes with negative stiffness resonators, Int. J. Mech. Sci. 261 (2024) 108668.
[40] Q. Lin, et al., Low-frequency locally resonant band gap of the two-dimensional quasi-zero-stiffness metamaterials, Int. J. Mech. Sci. 222 (2022) 107230.
[41] K. Wang, J. Zhou, D. Xu, H. Ouyang, Lower band gaps of longitudinal wave in a one-dimensional periodic rod by exploiting geometrical nonlinearity, Mech. Syst. Signal Process. 124 (2019) 664–678.
[42] R. Augello, E. Carrera, Nonlinear dynamics and band gap evolution of thin-walled metamaterial-like structures, J. Sound Vib. 578 (2024) 118329.
[43] A. Palermo, B. Yousefzadeh, C. Daraio, A. Marzani, Rayleigh wave propagation in nonlinear metasurfaces, J. Sound Vib. 520 (2022) 116599.
[44] Y. Shen, W. Lacarbonara, Nonlinearity enhanced wave bandgaps in metamaterial honeycombs embedding spider web-like resonators, J. Sound Vib. 562 (2023) 117821.
[45] W.J. Zhou, X.P. Li, Y.S. Wang, W.Q. Chen, G.L. Huang, Spectro-spatial analysis of wave packet propagation in nonlinear acoustic metamaterials, J. Sound Vib. 413 (2018) 250–269.
[46] C. Gong, X. Fang, L. Cheng, Band degeneration and evolution in nonlinear triatomic metamaterials, Nonlinear Dyn. 111 (2023) 97–112.
[47] Y. Xiao, J. Wen, D. Yu, X. Wen, Flexural wave propagation in beams with periodically attached vibration absorbers: band-gap behavior and band formation mechanisms, J. Sound Vib. 332 (2013) 867–893.
[48] Y. Xiao, J. Wen, X. Wen, Flexural wave band gaps in locally resonant thin plates with periodically attached spring–mass resonators, J. Phys. D Appl. Phys. 45 (2012) 195401.

[49] C. Li, T. Jiang, Q. He, Z. Peng, Stiffness-mass-coding metamaterial with broadband tunability for low-frequency vibration isolation, J. Sound Vib. 489 (2020) 115685.
[50] M. Yu, X. Fang, D. Yu, Combinational design of linear and nonlinear elastic metamaterials, Int. J. Mech. Sci. 199 (2021) 106422.
[51] G. Dhatt, E. Lefrançois, G. Touzot, Finite Element Method, John Wiley & Sons, 2012.
[52] G. Genta, Vibration Dynamics and Control, Springer, 2009.